

第 17 回 核燃焼プラズマ 統合コード研究会

17th Burning Plasma Simulation Initiative (BPSI) Meeting

日時：2019年12月5日(木)–6日(金)

場所：九州大学筑紫キャンパス

応用力学研究所 2階大会議室

(Ver. 1)



合同会合

第 17 回核燃焼プラズマ統合コード研究会

17th Burning Plasma Simulation Initiative (BPSI) Meeting

および

核融合エネルギーフォーラムサブクラスター会合
シミュレーションクラスター 炉心プラズマモデリングサブクラスター
プラズマ物理クラスター 定常運転・制御サブクラスター

(Ver.1)

日時：2019年12月5日(木)–6日(金)

場所：九州大学筑紫キャンパス 応用力学研究所 2階大会議室

12月5日(木)

9:15 – 9:25 はじめに 村上 (京大)

(座長：村上)

9:25 – 9:50 講演 1-1 本多 (量研)

Current status of the integrated model GOTRESS+

9:50 – 10:15 講演 1-2 仲田 (核融合研)

Global turbulent transport simulation using a coupled code TRESS+GKV

10:15 – 10:40 講演 1-3 登田 (核融合研)

Reduced model of turbulent transport for helical plasmas including effects of zonal flows and trapped electrons

10:40 – 10:55 休憩

(座長：糟谷)

10:55 – 11:20 講演 1-4 小菅 (九大)

Interplay among 3d flows in turbulent plasmas

11:20 – 11:35 講演 1-5 青木 (九大)

Neutral effects on the structure of minimum enstrophy flows in plasmas

11:35 – 11:55 講演 1-6 山本 (京大)

Effects of electron cyclotron heating on the toroidal flow in HSX plasmas

11:55 – 12:20 講演 1-7 村上 (京大)

Modeling of supra-thermal electron flux and toroidal torque by ECH in non-axisymmetric toroidal plasmas

12:20 – 12:30 議論

12:30 – 13:30 昼休み

(座長：林)

- 13:30 – 13:55 講演 2-1 相羽 (量研)
Impact of plasma rotation and ion diamagnetic drift effects on MHD stability in a QH-mode plasma
- 13:55 – 14:10 講演 2-2 富松 (九大)
Nonlinear dynamics of resistive ballooning instability in PLATO tokamak plasma
- 14:10 – 14:35 講演 2-3 矢木 (量研)
Particle transport model in plasma peripheral region
- 14:35 – 15:00 講演 2-4 矢本 (量研)
Study of multiple impurity seeding effect using SONIC integrated divertor code for JT-60SA plasma prediction
- 15:00 – 15:25 講演 2-5 大澤 (九大)
Stability of divacancy and interaction with inevitable impurities in metals
- 15:25 – 15:40 講演 2-6 下村 (九大)
Tungsten transport analysis using integrated code TASK
- 15:40 – 15:55 休憩

(座長：本多)

- 15:55 – 16:20 講演 2-7 糟谷 (九大)
Analysis of laboratory torus plasma using the integrated simulation scheme
- 16:20 – 16:45 講演 2-8 沼波 (核融合研)
Development of transport prediction scheme based on first-principle simulation and machine learning
- 16:45 – 17:10 講演 2-9 成田 (量研)
Neural-network-based multi-channel turbulent transport modeling
- 17:10 – 17:25 講演 2-10 森下 (京大)
Data assimilation system based on integrated transport simulation of LHD plasma
- 17:25 – 17:45 議論
- 17:45 散会
- 18:30 – 21:00 懇親会 (はるら 西鉄白木原駅近)

12月6日(金)

9:15 – 9:20 事務連絡

(座長：小菅)

9:20 – 9:45 講演 3-1 Chio Zong Cheng (東大)

TAEs and Alfvén-slow eigenmodes in tokamaks

9:45 – 10:10 講演 3-2 Fukuyama 福山 (京大)

Progress in wave heating and current drive using the TASK code

10:10 – 10:35 講演 3-3 Sasaki 佐々木 (九大)

Extraction of plasma turbulence dynamics by using dynamical mode decomposition

10:35 – 10:50 休憩

(座長：沼波)

10:50 – 11:15 講演 3-4 横山 (核融合研)

Modelling of thermal transport in fusion plasmas based on statistical approach

11:15 – 11:30 講演 3-5 太田 (京大)

Evaluation of the momentum dependence of radial diffusion coefficient on density and heat transport in tokamaks

11:30 – 11:50 議論

11:50 – 13:00 昼休み

(座長：藤田)

13:00 – 13:05 サブクラスター関係連絡・確認事項 林 (量研)

13:05 – 13:25 講演 4-1 宮戸 (量研)

IFERC 計算機シミュレーションセンターの現状報告

13:25 – 13:55 講演 4-2 本多 (量研)

ITER に於ける統合コード (IMEG) 活動報告

13:55 – 14:35 講演 4-3 若月、鈴木、林 (量研)

ITPA 統合運転シナリオグループ活動報告

14:35 – 14:45 休憩

(座長：打田)

14:45 – 15:25 講演 4-4 鈴木、林 (量研)

JT-60SA の研究活動報告

15:25 – 16:00 サブクラスター活動に関する総合討論と今後の予定 林 (量研)

16:00 散会

Current status of the integrated model GOTRESS+

M. Honda, N. Aiba, *H. Seto, E. Narita and N. Hayashi

*National Institutes for Quantum and Radiological Science and Technology, Naka,
Ibaraki 311-0193 Japan*

**National Institutes for Quantum and Radiological Science and Technology, Rokkasho,
Aomori 039-3212 Japan*

Recent progress in GOTRESS

Due to the sensitivity of turbulent fluxes to profile gradients, robust predictions are still arduous with a stiff turbulent transport model incorporated in a conventional transport code. To overcome this difficulty, we have developed a steady-state transport equation solver, GOTRESS, which benefits from global optimization techniques such as a genetic algorithm [1] and the Nelder-Mead method [2] such that they directly find the solution where a transport flux matches an integrated source [3]. In addition to quick calculation of steady-state profiles, GOTRESS has advantage to make it possible to deal with TGLF transport model [4], which is one of stiff transport models, in a robust manner on Multiple-Program Multiple-Data (MPMD) structure framework. Also, GOTRESS has an affinity for Machine-Learning techniques because it takes advantages of global optimization techniques that in typical produce a large amount of data, adequate for training of an artificial neural network model [5]. This surrogate model mimicking the behavior of an original model realizes rapid computation.

Novel integrated model GOTRESS+

A novel integrated model GOTRESS+ has been developed, mainly consisting of the equilibrium and current profile solver ACCOME and the neutral beam (NB) heating code OFMC, other than GOTRESS, for predictions of temperature profiles consistent with an equilibrium and heating profiles. A procedure of GOTRESS+ execution is described in the following. Figure 1 demonstrates a workflow of GOTRESS+ in the case of high-beta steady-state scenario in JT-60SA, what is called #5-1: $B_T = 1.72T$, $I_p = 2.3MA$,

$P_{NB} = 18.85\text{MW}$ and $P_{EC} = 7\text{MW}$ [6]. The settings of auxiliary heating systems such as NB heating and electron cyclotron heating (ECH) and the coils that support an equilibrium are described in an input file of ACCOME. The prescribed density and temperature profiles are also given as initial guess. After iterative calculations in ACCOME, a consistent solution is obtained between an equilibrium and a current profile according to the given kinetic profiles. At the same time, ACCOME also estimates ECH and EC current drive (ECCD), if needed. The profiles required for OFMC as input are sent to OFMC, and then the profiles of NB heating and NB current drive (NBCD) are estimated. Now the current density profiles, the equilibrium and heating profiles have been computed, which are all requisites for GOTRESS. GOTRESS in turn predicts the temperature profiles based on them. At this point, the first iteration of GOTRESS+ is completed, shown as "iteration 1" in fig. 1. The predicted temperature profiles are sent to ACCOME and replaces the prescribed ones used in the first iteration. The second iteration then commences. This iterative calculation continues until the profiles are well converged. For this case, all the profiles are converged after 6 iterations. The developed plasma meets the target values: the normalized beta of $4.42 > 4.3$, the energy

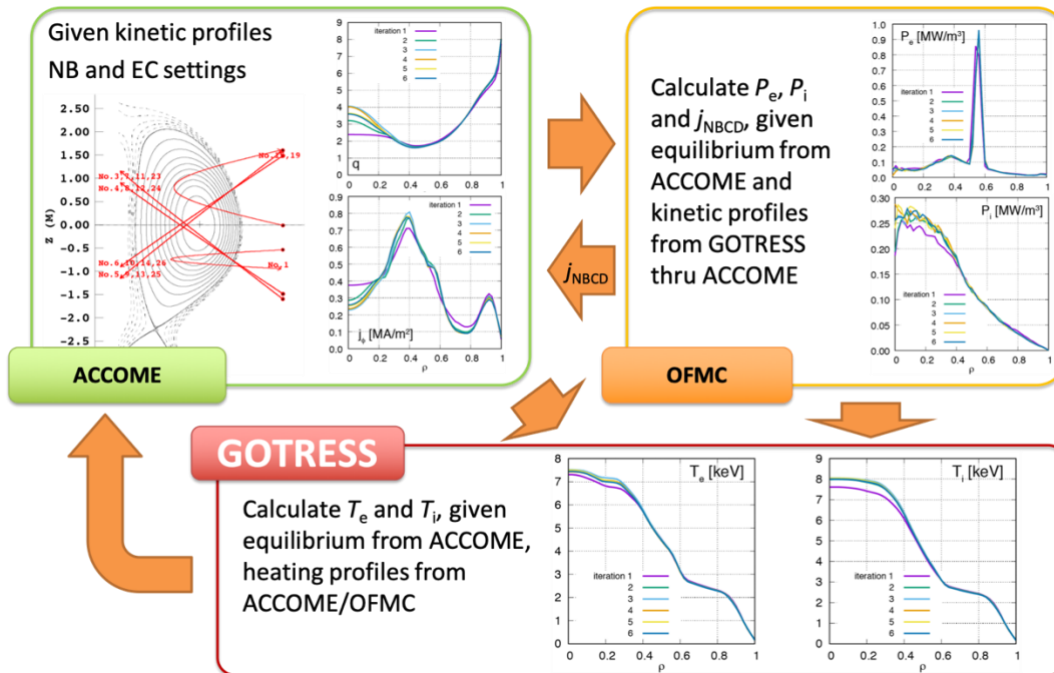


Fig. 1: Workflow of GOTRESS+. The predicted profiles are illustrated and each color of a line corresponds to the number of times of iteration.

confinement improvement of $1.65 > 1.3$ and the loop voltage of $0.003 \sim 0$.

We now compare steady-state profiles of the temperature and the heating power predicted by GOTRESS+ and TOPICS with the CDBM turbulent transport model exploited [7]. The boundary conditions were imposed at $\rho = 0.8$ in both simulations, where ρ is the normalized radial coordinate, so as not to include the pedestal because the physics governing the formation of the pedestal is different from that in the core region. Regardless of completely different numerical schemes used, both codes clearly predicted almost the same temperature profiles. The GOTRESS+ simulation took 6,812 seconds, around 10 hours faster than the TOPICS simulation. Thanks to the easy-to-use feature, GOTRESS readily makes it possible to lower the loop voltage much closer to nil by manipulating heating power carefully.

For more self-consistent predictions, estimation of the pedestal height and width is necessary. For this purpose, The EPED1 model has widely been used to predict pedestal height and width [8]. GOTRESS+ is now being extended to include our own EPED1 model that uses MARG2D, which is the ideal MHD stability code, replacing the ELITE code originally used in [8]. In EPED1, temperature profiles are scaled up/down if the initial ones render a plasma MHD stable/unstable and then an equilibrium is reevaluated using ACCOME. This process is repeated until the marginal stability condition is met. Coupling of GOTRESS+ and EPED1 is in progress.

References

- [1] P. Charbonneau, *Astrophys. J. Suppl. Ser.* **101** (1995) 309.
- [2] J. A. Nelder and R. Mead, *Computer J.* **7** (1965) 308.
- [3] M. Honda, *Comput. Phys. Commun.* **231** (2018) 94.
- [4] G. M. Staebler et al., *Phys. Plasmas* **12** (2005) 102508; *ibid.* **14** (2007) 055909.
- [5] M. Honda and E. Narita, *Phys. Plasmas* **26**, 102307 (2019).
- [6] N. Hayashi et al., *Proc. Int. Conf. on Fusion Energy (Ahmadabad, India, 2018)*, PPC/1-1 (2018).
- [7] M. Honda and A. Fukuyama, *Nucl. Fusion* **46** (2006) 580.
- [8] P. B. Snyder et al., *Phys. Plasmas* **16**, 056118 (2009).

Reduced models of turbulent transport including zonal flows and trapped electrons

S. Toda, M. Nunami, and H. Sugama

National Institute for Fusion Science, Oroshi-cho 322-6, Toki, Gifu, 509-5292, Japan

The quantitative prediction of the turbulent transport in toroidal plasmas is one of the most critical issues to be solved for realization of fusion energy. Recently, a large number of gyrokinetic simulations of the turbulent transport in toroidal plasmas have been performed. The gyrokinetic simulation results for tokamak and helical plasmas have been compared with the experimental observation results [1]. Since it is known that zonal flows can regulate the turbulent transport, numerous studies have been done to investigate the efficiency of zonal flows to improve plasma confinement in toroidal devices. In these studies, nonlinear gyrokinetic simulations have been performed to accurately determine the relation between the turbulent transport level and the zonal flow amplitude. However, such nonlinear simulations require a huge computational cost for the parameter scan in wide ranges of magnetic field configurations and plasma equilibrium profiles. To reduce the computational cost, the reduced models are proposed. These models can quickly predict the nonlinear simulation results of the turbulent transport coefficients and fluxes from the linear simulation results of the instabilities' growth rates and the zonal flow responses in helical plasmas under the conditions of adiabatic electrons [2] and kinetic electrons [3]. These reduced models are presented for the plasmas in the Large Helical Device (LHD), where the ion temperature gradient (ITG) modes are unstable. The turbulent and the zonal flow potential fluctuations can also be estimated by the reduced model derived from the linear simulation results. To evaluate turbulent electron particle and heat transport fluxes as well as for treating electromagnetic effects which become important for high- β plasmas, kinetic electrons need to be treated in linear and nonlinear gyrokinetic simulations. In particular, in helical plasmas, trapped electrons show complicated drift motions and it is a serious challenge to quantitatively clarify how they impact instabilities, zonal flows, and turbulent transport. In this study, effects of trapped electrons on zonal flows and turbulent transport in the LHD configuration are studied. The residue zonal flow level for the case of kinetic electrons is compared with that in the adiabatic electron condition by the linear gyrokinetic simulation for the plasmas in the LHD, where the ITG mode is unstable. The residue level of zonal flows has been studied in tokamak and helical plasmas by the gyrokinetic simulations. In addition, the zonal flow decay time for the kinetic electron case is compared with that in the adiabatic electron condition. Next, evaluating the mixing length estimate and the zonal flow decay time by the linear gyrokinetic simulations, the saturation levels of turbulence and zonal flows are predicted from the reduced transport models with setting different field configurations and plasma equilibrium profiles for which effects of electrons on zonal flows and plasma confinement are investigated.

The turbulence driven by the microinstabilities and zonal flows in the LHD plasmas are studied, using the gyrokinetic local flux tube code, GKV [4]. In this study, the diffusivity and quasilinear flux models [2, 3] for the ion heat transport are used for the adiabatic electron condition and the kinetic electron condition. These reduced models are constructed, where the ITG mode is unstable. The models for the electrostatic turbulent and zonal flow potential fluctuations are also used. The electron density perturbation δn_e is given in terms of the electrostatic potential fluctuation by

$$\frac{\delta n_{e, \tilde{k}_x, \tilde{k}_y}}{n_0} = \begin{cases} e \left[\tilde{\phi}_{\tilde{k}_x, \tilde{k}_y} - \langle \tilde{\phi}_{\tilde{k}_x, \tilde{k}_y} \rangle \right] / T_e & \text{if } \tilde{k}_y = 0 \\ e \tilde{\phi}_{\tilde{k}_x, \tilde{k}_y} / T_e & \text{if } \tilde{k}_y \neq 0, \end{cases} \quad (1)$$

where e is the elementary charge, n_0 is the background density, T_e is the electron temperature, $\tilde{\phi} = \phi / ((T_i/e)(\rho_i/R))$, R is the major radius and $\rho_i (= m_i v_{ti} / (eB))$ is the thermal ion gyroradius. Here, m_i is the ion mass, B is the magnetic field strength, $v_{ti} (= \sqrt{T_i/m_i})$ is the thermal ion velocity and T_i is the ion temperature. The average along the field line is denoted by $\langle \dots \rangle$ and $\tilde{k}_x (= k_x \rho_i)$ and $\tilde{k}_y (= k_y \rho_i)$ are the normalized radial and poloidal wavenumbers, respectively. Only pure ITG modes are treated by the adiabatic electron response for $\tilde{k}_y \neq 0$. For $\tilde{k}_y = 0$, the so-called modified adiabatic electron response is assumed. The models for the squared turbulent and zonal flow potential fluctuations, $\mathcal{T} \left(= \sum_{\tilde{k}_x, \tilde{k}_y \neq 0} \left\langle |\tilde{\phi}_{\tilde{k}_x, \tilde{k}_y}|^2 \right\rangle / 2 \right)$ and $\mathcal{Z} \left(= \sum_{\tilde{k}_x} \left\langle |\tilde{\phi}_{\tilde{k}_x, \tilde{k}_y=0}|^2 \right\rangle / 2 \right)$ are also represented by the linear simulation results, to reproduce the nonlinear simulation results. The major radii of the plasmas are given by $R = 3.75\text{m}$ for the standard field configuration and $R = 3.6\text{m}$ for the inward-shifted field configuration. The abbreviations *SD* and *IW* used in this study stand for the standard and inward shifted field configurations, respectively. The linear zonal flow response function is defined by $\mathcal{R}_{\tilde{k}_x}(t) \equiv \left\langle \tilde{\phi}_{\tilde{k}_x, \tilde{k}_y=0}(t) \right\rangle / \left\langle \tilde{\phi}_{\tilde{k}_x, \tilde{k}_y=0}(t=0) \right\rangle$. Note that the zonal flow response function for $\tilde{k}_x = 0.25$ is used to evaluate the representative values of the zonal flow decay time, because there are peaks of the wavenumber spectra around $\tilde{k}_x = 0.25$ in the nonlinear simulation results. To study the correlation between $\mathcal{R}_{\tilde{k}_x}(t)$ and the fluctuation of zonal flows $\tilde{\mathcal{Z}}$, the zonal flow decay time is employed. The normalized zonal flow decay time is defined as $\tilde{\tau}_{ZF} = \tau_{ZF} / (R/v_{ti})$. The helical magnetic structure in the inward-shifted field configuration enhances the zonal flow generation.

The linear simulation results related with zonal flows for the modified adiabatic electron (MAE) condition of (1) are compared with those for the case of the kinetic electron (KE) response in the SD and IW. The decay time of zonal flows depends on the magnetic field configuration and is independent of the density and temperature profiles. When the field configuration model was used, it was analytically shown that the linear response function decays faster due to the presence of the trapped particles than for the MAE condition. It was found that the residue level for zonal flows complicatedly depends on the helical ripple and the ratio of the neoclassical polarization due to toroidally trapped particles to the classical polarization. The linear zonal flow response function for the case of the KE response is confirmed to decay faster than that for the MAE response in the SD and IW. The residue level of zonal flows for the case of the KE response is smaller than that for the MAE response in the SD at $\rho = 0.65$. This tendency is the same in the SD at $\rho = 0.80$. However, it is clarified that the residue levels are found to be almost the same for the MAE and KE conditions at $\rho = 0.65$ in the IW. For comparing the zonal flow decay time for the case of the KE response with that for the MAE condition, the value of τ_f is set to be $30R/v_{ti}$ for the MAE and KE conditions. The zonal flow decay time is larger for the MAE condition than for the KE condition in the SD. However, the zonal flow decay time for the KE condition is found to be comparable to or slightly larger than that for the MAE condition in the IW. The difference of the magnitude relationship of the residue level for zonal flows or the zonal flow decay time in the SD and IW is due to the complicated dependence on the helical ripple and the effect of the toroidally trapped particles.

The nonlinear simulation results, such as the ion heat diffusivity, χ_i as well as the turbulent and the zonal flow potential fluctuations, $\tilde{\mathcal{T}}$ and $\tilde{\mathcal{Z}}$, are predicted by the models. The model predictions for the case of the KE response are compared with those for the adiabatic electron (AE) condition. The values of $\tilde{\mathcal{T}}$ for the case of the KE response are found to be larger than those for the AE condition in both field configurations, because the trapped electron enhances the growth rate of the ITG. Turbulence potential fluctuations in the IW are close to that in the SD.

The models can predict the nonlinear simulation results for $\bar{\mathcal{T}}$, except for the region $\rho < 0.6$ in the IW. The zonal flow potential fluctuation, $\bar{\mathcal{Z}}$ in the IW is found to become larger than that in the SD, especially for the case of the KE response. The simulation result confirms that zonal flow potential fluctuation in the IW is larger than that in the SD. The model for $\bar{\mathcal{Z}}$ reproduces the nonlinear simulation results in the SD. The model does not predict the nonlinear simulation results especially for the case of the KE response in the IW, because the plasma profile in the SD is not used for the IW simulation for constructing the model for $\bar{\mathcal{Z}}$. In the SD, the zonal flow effect is stronger for the MAE condition than for the KE condition. On the other hand, in the IW, the zonal effect for the case of the KE response is comparable to that for the MAE condition. The linear simulation results are qualitatively reflected in these nonlinear simulation results for the zonal effect. It is clarified that the reduced models reproduce the nonlinear simulation results. Even if the linear and nonlinear simulation results in the IW using the plasma profiles in the SD were not adapted for constructing the reduced models for the case of the KE response, the reduced model can reproduce the nonlinear simulation results in the IW for the case of the KE response. It is found that the transport predicted by the reduced models in the IW is smaller than that in the SD. Effects of trapped electrons on zonal flows and turbulent transport in two kinds of LHD field configurations are studied for the representative plasmas, where the ITG mode is unstable. For the linear simulation results, the residue level and the decay time of zonal flows for the case of the kinetic electron response is smaller than for the modified adiabatic electron response in the SD field configuration. However, the residue level and the decay time of zonal flows for the case of the kinetic electron response are found to be comparable to those for the modified adiabatic electron response in the IW shifted field configuration. For the predictions of the reduced models, the zonal flow effect on the transport for the case of the kinetic electron response is weaker than that for the adiabatic electron response in the SD field configuration. In the IW shifted configuration, the zonal flow effect for the case of the kinetic electron response is found to be comparable to that for the adiabatic electron response. The zonal flow effect on the transport depends on not only the zonal flow decay time but also the mixing length estimate in the reduced models. The ion heat diffusivities predicted by the reduced model in the IW shifted field configuration are smaller than those in the SD field configuration. It is found that the linear simulation result, such as the zonal flow decay time, is the possible qualitative criterion for zonal flow effect on the transport. The nonlinear simulation results are well reproduced by the reduced models for the heat diffusivity and the quasilinear flux model, even in the parameter region for the case of the kinetic electron response in the IW shifted field configuration, where the data for the heat transport are not used for constructing the reduced models. This work was partly supported by the NIFS Collaboration Research Programs, NIFS18KNST129 and NIFS18KNXN363 (Plasma Simulator), NIFS18KNTT045, and the Collaborative Research Program of Research Institute for Applied Mechanics, Kyushu University, 2019FP-4.

- [1] S. Toda et al., Plasma and Fusion Research **14**, 3403061 (2019).
- [2] M. Nunami, T. -H. Watanabe and H. Sugama, Phys. Plasmas **20**, 092307 (2013).
- [3] S. Toda et al., Phys. Plasmas **26**, 012510 (2019).
- [4] T. -H. Watanabe and H. Sugama, Nucl. Fusion **46**, 24 (2006).

Flow helicity of wavy plasma turbulence

Y. Kosuga^[1,2]

[1] Research Institute for Applied Mechanics, Kyushu University, Fukuoka, Japan

[2] Research Center for Plasma Turbulence, Kyushu University, Fukuoka, Japan

Helicity of flow field, defined as $\mathbf{v} \cdot \boldsymbol{\omega}$ where \mathbf{v} is the velocity and $\boldsymbol{\omega} = \nabla \times \mathbf{v}$ is the vorticity, is an important quantity to understand the dynamics of turbulent plasmas. For example, turbulence with finite flow helicity can transport momentum to generate large scale flows. Turbulence with finite helicity also can generate large scale magnetic field, which can be modelled via the famous alpha term in the mean field theory of the magnetic field evolution. Moreover the generation of large scale helical flows is reported from theory[1] and numerical simulation[2]. Flow helicity plays an important role to quantify the resultant flow structures.

In this work[3], we have analyzed how the helicity of turbulent plasmas is determined, by using drift wave turbulence and parallel velocity gradient driven (PVG) turbulence. First of all, we identify relevant symmetry breaking to have the flow helicity to be finite. Generally, the helicity of the flow field is finite when the reflectional symmetry is broken in the system. In the case of magnetized plasmas, we find that the breaking of the reflectional symmetry is closely related to the breaking of the symmetry along the magnetic field. In this regard, PVG turbulence is a typical example of the turbulence with finite flow helicity, since the growth is asymmetric with regard to the direction of the magnetic field. For the given parallel flow shear and the poloidal mode number, fluctuation with the particular sign of the parallel wave number is excited. This translates into the helicity of PVG turbulence as

$$\langle \tilde{\mathbf{v}} \cdot \tilde{\boldsymbol{\omega}} \rangle = 2 \frac{c}{B} \langle \tilde{v}_z \nabla_{\perp}^2 \tilde{\phi} \rangle = 2 c_s \omega_{ci} \frac{c_s / L_n}{\langle v_z \rangle'} \sum_k k_{\perp}^2 \rho_s^2 \left| \frac{e \tilde{\phi}_k}{T_e} \right|^2 \quad (1)$$

Thus the helicity of PVG turbulence, especially the entire sign, is determined by $\propto \langle n \rangle' \langle v_z \rangle' B$. Then flipping the magnetic field or the parallel flow direction, the sign of the helicity flips. Pictorially, turbulence may be filled with the lefthanded helix, while by flipping these signs the turbulence can be filled with the righthanded helix.

Then the dynamical evolution of fluctuation helicity is formulated. Especially we emphasized the link of the evolution of fluctuation helicity to the transport fluxes. For PVG turbulence, the relevant flux to drive the fluctuation helicity evolution is tied to the momentum flux of parallel flows. Note that the parallel momentum flux requires the symmetry breaking to have a finite value. The finiteness of this flux is tied to the finiteness of the fluctuation helicity, which is a plausible result. Then the obtained evolution equation is used to diagnose the simulation data obtained from the NLD code. A steady state balance is achieved by balancing the damping of helicity and the parallel momentum flux. The resultant expression has the similar dependence on the sign as Eq.(1).

Stimulating discussion with P.H. Diamond, K. Itoh, S. Inagaki, F. Kin, is acknowledged. This work was supported by Grants-in-Aid for Scientific Research of JSPF of Japan (JP15H02155, JP17H06089, JP18K03578), the Joint research project in RIAM.

References

- [1] Y. Kosuga, S.-I. Itoh and K. Itoh, Phys. Plasmas **24** 032304 (2017)
- [2] M. Sasaki, N. Kasuya, K. Itoh, S. Toda, T. Yamada, Y. Kosuga, Y. Nagashima, T. Kobayashi, H. Arakawa, K. Yamasaki, A. Fujisawa, S. Inagaki, and S.-I. Itoh, Phys. Plasmas **24** 112103 (2017)
- [3] Y. Kosuga, M. Sasaki, Z.B. Guo Phys. Plasmas **27** 022303 (2020)

Effects of Electron Cyclotron Heating on the Toroidal Flow in HSX Plasmas

Y. Yamamoto, S. Murakami, S.T.A. Kumar*, J.N. Talmadge*, K.M. Likin*, D.T. Anderson*,

Department of Nuclear Engineering, Kyoto Univ., Nishikyo, Kyoto 615-8540, Japan

** Department of Electrical and Computer Engineering, University of Wisconsin-Madison, Madison, WI 53706, USA*

e-mail: yamamoto_y@p-grp.nucleng.kyoto-u.ac.jp

The toroidal flow related to electron cyclotron heating (ECH) is investigated in HSX plasmas. Radial diffusion of energetic electrons by ECH produces a canceling return current, which then generates a $j_r \times B$ torque that can play an important role in the toroidal rotation in ECH plasma. We investigate the energetic electron distribution by ECH by applying GNET code, which can solve the 5D drift kinetic equation for the energetic electron. We evaluate the $j_r \times B$ torque and the collisional torque due to the friction of the toroidal drift motion of the energetic electrons. As a result, we obtained a significant torque due to the ECH and found that a larger torque is obtained in the Mirror configuration than in the quasi-helically symmetric (QHS) configuration in HSX. Solving the momentum balance equations and Ampère’s law with the $j_r \times B$ torque, we evaluate the toroidal flow velocity and compare simulations with HSX experiments. The obtained flows have good agreement with experimental ones.

Introduction

Recently, spontaneous toroidal flows have been observed in electron cyclotron heating (ECH) plasmas in many tokamak and helical devices such as JT-60U, LHD and HSX. To clarify the underlying mechanism, many experimental [1] and theoretical studies have been undertaken. The effects of the magnetic configuration on plasma flow are intensively investigated in HSX, where two typical magnetic configurations are considered. One is the Quasi-Helically Symmetric (QHS) configuration, which has a quasi-helical symmetry in $|B|$ and is dominated by the $[m, n] = [1, 4]$ mode. The other is the Mirror configuration, where a set of auxiliary coils adds toroidal mirror terms, the (0, 4) and (0, 8) modes, to the magnetic field spectrum to break the helical symmetry. The QHS configuration has a parallel neoclassical viscosity that is smaller than that of the Mirror configuration, so we expected that the toroidal flow velocity in the QHS configuration would be larger than that of the Mirror configuration. However smaller toroidal flow was observed in the QHS configuration. It has not been understood well yet.

Simulation model

ECH can drive the radial electron current j_e due to the radial motion of suprathermal electrons [2]. The net current in the steady state should be canceled to maintain the quasi-neutrality, so the return current, $j_r (= -j_e)$, must flow by the bulk ions by ambipolar condition. Therefore, the bulk plasma feels the $j_r \times B$ torque due to the return current. On the other hand, the suprathermal electrons drift toroidally due to the precession motion. During the slowing down of the suprathermal electrons, they transfer their obtained momentum to the bulk plasma due to collisions.

In this study, we investigate the behaviors of energetic electrons by ECH, which can generate the radial current making the $j_r \times B$ torque in the HSX plasmas. Also, we evaluate the collisional torques, by the collision between energetic electrons and bulk plasma. We apply the GNET code,

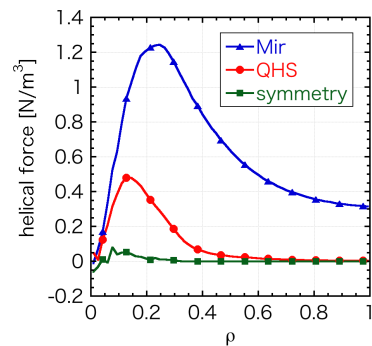


Figure 1: *The total helical forces including $j_r \times B$ and collisional torques in three configurations.*

which can solve a linearized drift kinetic equation for energetic electrons by ECH in 5-D phase space[2]

$$\frac{\partial \delta f}{\partial t} + (\vec{v}_d + \vec{v}_{\parallel}) \cdot \frac{\partial \delta f}{\partial \vec{r}} + \dot{v} \cdot \frac{\partial \delta f}{\partial \vec{v}} - C(\delta f) - L(\delta f) = S^{\text{ql}}(f_{\text{Max}}).$$

Solving the momentum balance equations and Ampère's law with the radial electron flux and torques, we evaluate the toroidal flow velocity and compare them with experimental one.

Results

In the perfectly symmetric configuration, the forces in the symmetry direction cancel each other. As seen in Fig.1, the $j_r \times B$ torque and the collisional torque cancel each other and the component parallel to the helically symmetry direction is very small in the perfectly helically symmetric configuration[3]. However non-symmetric magnetic modes enhance the radial current j_e . Thus, even in the QHS configuration the $j_r \times B$ torque is dominant and there is a net force in the symmetry direction due to other small non-symmetric modes. The force in Mirror configuration is more than twice as large as that in QHS configuration with the same input power. The collisional torque is so small that we can ignore it in QHS and Mirror configurations. Solving the momentum balance equations with $j_r \times B$ torque, the obtained flow velocity is shown in Fig.2. Here the absorption power calculated by ray-tracing code is 24kW in QHS configuration and 16kW in Mirror configuration. The obtained flow in QHS configuration is strongly peaked, but the toroidal flow in Mirror configuration is larger than that in QHS configuration totally.

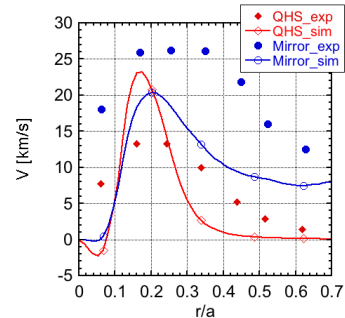


Figure 2: *The obtained toroidal flow in QHS and Mirror configurations. The lines are simulation results and the dots are experimental ones.*

- [1] S.T.A. Kumar, et al., Nucl. Fusion **60** (2018) 054012.
- [2] S. Murakami, et al., Nucl. Fusion **40** (2000) 693.
- [3] Y. Yamamoto, et al., Plasma and Fusion Research **14** (2019) 3403105
- [4] M. N. Rosenbluth and F. L. Hinton, Nucl. Fusion **36** (1996) 55

Impacts of plasma rotation and ion diamagnetic drift on MHD stability in a QH-mode plasma

N. Aiba^{1*}, X. Chen², T. H. Osborne², S. R. Haskey³, K. H. Burrell², P. B. Snyder²

¹ *National Institutes for Quantum and Radiological Science and Technology, Naka, Ibaraki 311-0105, Japan*

² *General Atomics, PO Box 85608, San Diego, CA 92186-5608, USA*

³ *Princeton Plasma Physics Laboratory, PO Box 451, Princeton, NJ 08543-0451, USA*

* Email address of submitting author: aiba.nobuyuki@qst.go.jp

In H-mode regime in tokamaks, edge localized modes (ELMs) often appear and induce large heat load to divertors. Since the heat load is unacceptable for future large reactors like ITER and DEMO, it is necessary to suppress and/or mitigate the ELMs. Quiescent H-mode (QH-mode) is one of the promising candidates realizing ELM suppression and high confinement performance with ITER and DEMO relevant plasma parameters [1]. One of the important characteristics of the QH-mode is that edge harmonics oscillations (EHOs) are observed, though ELMs disappear. Since QH-mode can be obtained when bootstrap current and rotation shear near plasma surface are large, the EHOs have been recognized as a rotation shear destabilized current-driven MHD (peeling) mode. The hypothesis has been validated by linear analyses with the ideal [2] and resistive [3] MHD models.

In addition, the ion diamagnetic drift frequency, ω_{*i} , can be comparable to the plasma rotation frequency [3], hence, the $E \times B$ rotation has been recognized as a strong candidate responsible for entering QH-mode, the rotation which is composed of the sum of plasma fluid rotation and the ion diamagnetic drift [4]. The MHD analysis with the $E \times B$ rotation as already performed in [3], however, in this case, the ion diamagnetic drift was treated as the single fluid MHD rotation. The stabilizing effect by the ion diamagnetic drift on pressure-driven ballooning mode in a static plasma has long been recognized as discussed in [5], and the effect has been obtained by treating the fluid rotation and the ion diamagnetic drift independently.

In this study, we analyze numerically the MHD stability in DIII-D QH-mode plasmas by considering plasma rotation and ω_{*i} effects simultaneously with the linear extended MHD stability code MINERVA-DI [6]. This code solves the extended Frieman-Rosenbluth (F-R) equation

$$\rho_0 \frac{\partial^2 \xi}{\partial t^2} + 2\rho_0 (\mathbf{V}_{0,MHD} \cdot \nabla) \frac{\partial \xi}{\partial t} + \rho_0 (\mathbf{V}_{0,*i} \cdot \nabla) \frac{\partial \xi_{\perp}}{\partial t} = F(\xi),$$

$$\nabla \cdot \xi = 0$$

with the definition of velocity vectors as

$$\mathbf{V}_{MHD} = \mathbf{V}_{\perp} + \frac{V_{\parallel} \mathbf{B}}{|\mathbf{B}|},$$

$$\mathbf{V}_{*i} = \frac{1}{e \bar{Z} N |\mathbf{B}|^2} \mathbf{B} \times \nabla p_i,$$

where $F(\xi)$ is the linearized force operator derived from the diamagnetic MHD model [6]. Here $\xi = \xi_{\perp} + \xi_{\parallel} \mathbf{B}/|\mathbf{B}|$ is the Lagrangian displacement vector defined with the linearized Eulerian velocity, ρ is the plasma mass density, e is the quantum of electricity, \bar{Z} is the ion mean charge satisfying $N_e = \bar{Z} N_i$, N_e (N_i) is the electron (ion) number density, p_i is the ion pressure, and the subscript 0 indicates the equilibrium quantity.

The analyzed DIII-D plasma is #153440, which has the EHO with the large $n=2$ component in magnetic fluctuation, where n is the toroidal mode number. The parameters of this plasma are the toroidal magnetic field $|B_t| \sim 1.91T$, the plasma current $|I_p| \sim 1.5MA$, B_t and I_p are clockwise from the top view of the torus, the ellipticity $\kappa \sim 1.85$, and the triangularity $\delta \sim 0.5$. As discussed in [3,4], the rotation shear is not the toroidal rotation of impurity (carbon) but the toroidal rotation associated with the $E \times B$ drift, $\omega_{E \times B}$, is thought to be responsible for

entering the QH-mode, hence, the MHD stability is analyzed by taking into account $\Omega_{E \times B}$. Note that such the analysis can be realized by setting $V_{0,MHD} = R\omega_\phi - r\omega_\theta B_t/|B_\theta| = R\omega_{v \times B}$, because the ion diamagnetic drift frequency in $\omega_{E \times B}$ is explicitly included as $V_{0,*i}$ in the extended F-R equation. Here Ω_ϕ (Ω_θ) is the rotation frequency in the toroidal (poloidal) direction, r is the plasma minor radius, and B_p is the poloidal magnetic field. The ω_ϕ and ω_θ profiles are determined by using the measured rotation profiles of carbon, $\omega_{\phi,C}$ and $\omega_{\theta,C}$, and the corresponding $\omega_{v \times B}$ is named as $\omega_{v \times B,C}$. The ion diamagnetic drift frequency ω_{*i} profile is evaluated with both the deuterium and carbon pressure profiles with the assumption that the temperature is the same as each other. The equilibrium profiles of the plasma are shown in Fig.1.

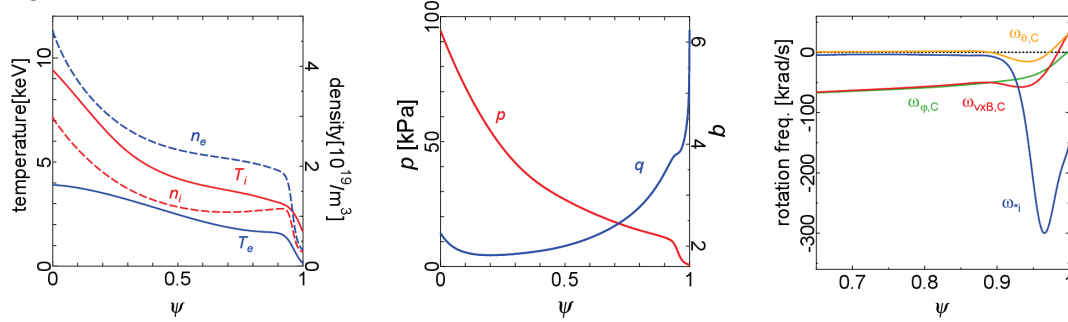


Fig.1 Profiles of the DIII-D 153440/1.724sec. plasma; (left) T_i , T_e , N_i , N_e , (center) P_0 , q , (right) $\omega_{\phi,C}$, $\omega_{\theta,C}$, $\omega_{v \times B,C}$, ω_{*i}

Figure 2 shows the stability diagram of the plasma on the $j_{ped} - \alpha$ plane, where j_{ped} is the flux averaged current density inside edge pedestal, and α is the normalized pressure gradient. When analyzing the stability without the ω_{*i} effect, the stability boundary indicates that the current driven MHD mode (kink/peeling mode) is destabilized by rotation because the mode can be unstable with small amount of j_{ped} as shown in Fig.2(a). The trend is consistent with the previous results discussing the impact of sheared rotation on kink/peeling mode stability. However, when considering the ω_{*i} effect simultaneously, the kink/peeling mode in rotation plasmas requires large amount of j_{ped} for destabilization as shown in Fig.2(b). Namely, the rotation stabilizes

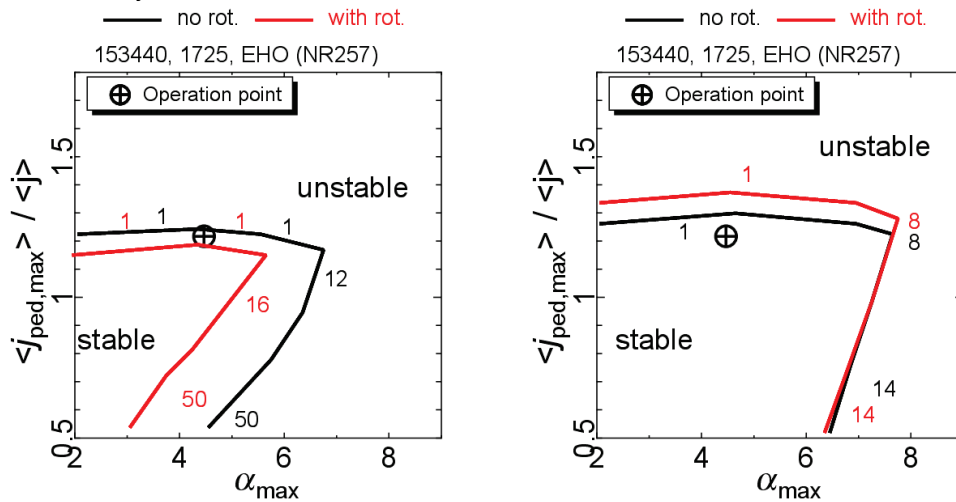


Fig.2 MHD stability diagram of the DIII-D 153440/1.725sec. QH-mode plasma on the $j_{ped} - \alpha$ diagram; the target expresses the equilibrium values observed in experiment, and the numbers on the thagram show the toroidal mode number of the MHD mode determining the stability boundary; (left) without ω_{*i} , (right) with ω_{*i} .

the king/peeling mode. The trend is clearly observed when varying the rotation profile by multiplying coefficient C to $\omega_{v \times B, C}$; the result is shown in Fig.3. As shown in this figure, the stability boundary of the peeling modes slightly moves downward by increasing $\omega_{v \times B, C}$, because the mode is destabilized. On the other hand, when including both rotation and the ω_{*i} effects, the boundary moves upward; namely the mode is stabilized by rotation.

These results imply that the rotation effect on kink/peeling mode stability depends on the existence of the ion diamagnetic drift effect. Since the ion diamagnetic drift at edge pedestal region in QH-mode plasmas is usually large, both effects could play key roles for entering QH-mode. To validate this numerically, nonlinear simulation including both the effects is necessary to obtain QH-mode plasma numerically as a steady state with EHOs. This remains as our future work.

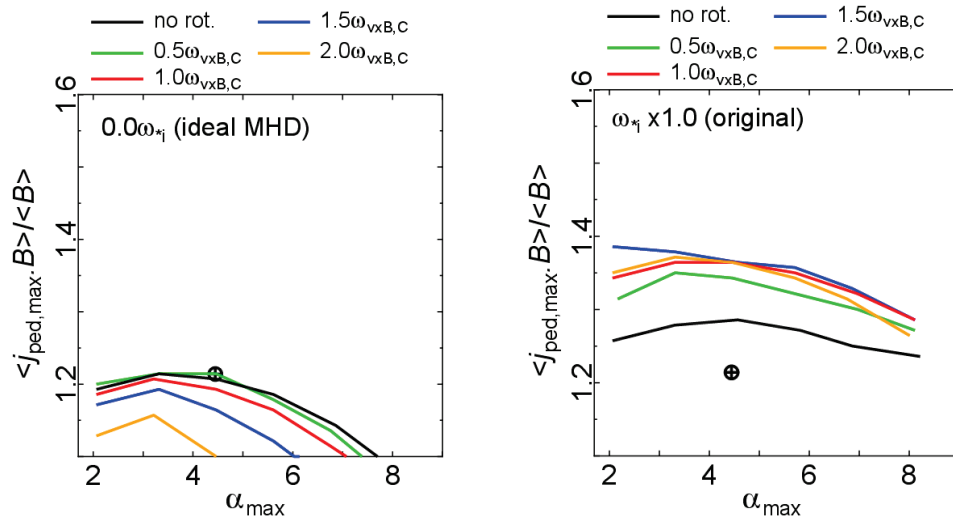


Fig.3 Impact of rotation frequency, $C\omega_{v \times B, C}$, on the kink/peeling mode stability boundary on the $j_{ped} - \alpha$ diagram; (left) without ω_{*i} , (right) with ω_{*i} .

This material is based upon work supported by the U.S. Department of Energy, Office of Science, Office of Fusion Energy Sciences, using the DIII-D National Fusion Facility, a DOE Office of Science user facility, under Awards DE-FC02-04ER54698. DIII-D data shown in this paper can be obtained in digital format by following the links at https://fusion.gat.com/global/D3D_DMP.

- [1] K. H. Burrell et al., PRL 102, 155003 (2009).
- [2] T. H. Osborne et al., J. Phys. Conf. Ser. 120 012014 (2008).
- [3] X. Chen et al., Nucl. Fusion 56 076011 (2016).
- [4] A. Garofalo et al., Nucl. Fusion 51 083018 (2011).
- [5] M. S. Chu et al., Phy. Rev. Lett. 41 247 (1978) etc..
- [6] N. Aiba, PPCF 58, 045020 (2016).

Nonlinear dynamics of resistive ballooning instability in PLATO tokamak plasma

S. Tomimatsu¹, N. Kasuya^{1,2}, M. Sato³, A. Fukuyama⁴, M. Yagi⁵, Y. Nagashima^{1,2},
and A. Fujisawa^{1,2}

¹IGES, Kyushu University, ²RIAM, Kyushu University, ³NIFS, ⁴Kyoto University, ⁵QST

1. Introduction

In order to realize a fusion reactor, it is necessary to sustain stable confinement of high-temperature plasmas. However, in a torus plasma, there are various instabilities that have their characteristic spatial-temporal scales (e.g. MagnetoHydroDynamics (MHD), ion and electron scales), and these instabilities make it difficult to confine the plasma [1,2]. MHD instabilities due to the pressure gradient and the plasma current cause plasma collapse phenomena [3-5]. Therefore, understanding the characteristics of MHD instabilities is essential for stable control of plasma performance.

In order to understand the physical mechanism of plasma dynamical phenomena, laboratory size tokamak PLATO is now under construction in Kyushu university to make detailed measurements of plasma perturbations by using various experimental diagnostics [6]. The flexible design of PLATO tokamak makes it possible to observe dynamics of 3-D turbulence structures. The expected plasma parameters of PLATO tokamak parameters are following; major radius $R = 0.7\text{m}$, minor radius $a = 0.2\text{m}$, plasma volume $V_p = 0.9\text{m}^3$, electron temperature $T_e = 0.2\text{keV}$, density $n = 1.0 \times 10^{19}\text{m}^{-3}$.

In this study, the target is MHD instabilities with macro scales, and we carry out MHD simulations by using PLATO tokamak parameters to represent dynamics of MHD instabilities in a tokamak plasma. Ballooning and kink modes are induced depending on the safety factor q profile and the steep gradient region, and pressure flattening processes accompanied with competition of instabilities are investigated in the nonlinear dynamics.

2. Equilibrium in PLATO

The plasma equilibria considering the experimental conditions are evaluated by using the module EQU in integrated transport code TASK [7]. TASK/EQU calculates equilibria with free boundary conditions in existence of external vertical coils [8]. Figure 1 shows the magnetic configuration obtained by using the set of external coil currents. In this calculation, only D, H and Q coils are used for control parameters. This calculation gives toroidal magnetic field $B_t = 0.3\text{T}$, plasma current $I_p = 40\text{kA}$, central-beta $\beta_t = 2\%$, central- q $q_{\text{axis}} = 0.7$, surface- q $q_{\text{surf}} = 9.8$, ellipticity $\kappa = 1.6$ triangularity $\delta = 0.3$.

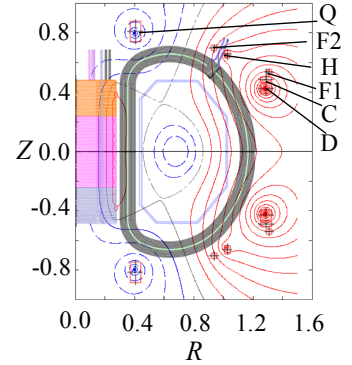


Fig.1 Magnetic configuration obtained by TASK/EQU. The configuration has up-down symmetry.

3. MHD simulation

For simulations of MHD instabilities in PLATO tokamak, MIPS code [9] is used. MIPS code solves the MHD equations described below in the cylindrical coordinates (R, Z, ϕ) ;

$$\rho \frac{\partial \vec{v}}{\partial t} = \rho \vec{\omega} \times \vec{v} - \rho \nabla \left(\frac{v^2}{2} \right) - \nabla p + \vec{j} \times \vec{B} + \frac{4}{3} \nabla [v \rho (\nabla \cdot \vec{v})] - \nabla \times [v \rho \vec{\omega}], \quad (1)$$

$$\frac{\partial \rho}{\partial t} = -\nabla \cdot (\rho \vec{v}), \quad (2)$$

$$\frac{\partial \vec{B}}{\partial t} = -\nabla \times \vec{E}, \quad (3)$$

$$\vec{E} = -\vec{v} \times \vec{B} + \eta \vec{j}, \quad (4)$$

$$\vec{j} = \frac{1}{\mu_0} \nabla \times \vec{B}, \quad (5)$$

$$\vec{\omega} = \nabla \times \vec{v}. \quad (6)$$

$$\begin{aligned} \frac{\partial p}{\partial t} = & -\nabla \cdot (p\vec{v}) - (\gamma - 1)p\nabla \cdot \vec{v} + \chi \nabla^2 (p - p_{eq}) \\ & + (\gamma - 1) \left[\nu \rho \omega^2 + \frac{4}{3} \nu \rho (\nabla \cdot \vec{v})^2 + \eta \vec{j} \cdot (\vec{j} - \vec{j}_{eq}) \right], \quad (7) \end{aligned}$$

Here, ρ , p , \vec{v} , \vec{B} , \vec{E} , \vec{j} are the mass density, plasma pressure, velocity, magnetic field, electric field and current density, p_{eq} , \vec{j}_{eq} are the equilibrium pressure and current, respectively. ν , η , γ , χ are viscosity, resistibility, adiabatic constant and thermal diffusion coefficient, and $\nu = \eta/\mu_0 = 10^{-5}v_a R_0$, $\chi = 10^{-7}v_a R_0$ are used for the following calculations, where v_a is the Alfvén velocity, $R_0 = 0.7$ m is the typical major radius. The time t is normalized by the Alfvén time.

The MHD equilibria used in the simulations are constructed by TASK/EQ module which calculates equilibria with a fixed boundary condition. The magnetic surface of $q = 5.5$ of the equilibrium calculated by the TASK/EQU module shown in Fig.1 is used for the boundary condition of the TAKS/EQ module.

Figure 2 shows the time evolution of the pressure perturbation energy for $q_{axis} = 0.8$, where the pressure is normalized by B_0^2/μ_0 . The total pressure perturbation energy, which is integrated for the whole plasma volume, increases monotonically in the linear phase, and show nonlinear saturation after the phase. Its Fourier decomposition to the toroidal components is also shown in Fig. 2. The initial growth rate of the $n = 1$ component is smaller than that of the $n = 14$ component, where n is the toroidal mode number. The growth rate of the $n = 1$ component increases at $t = 300$, and at $t = 500$ its magnitude becomes larger than those of the other modes. The pressure components in the poloidal cross-section are shown in Figs. 3. In Fig. 3 ($t = 300$), a ballooning mode structure whose perturbation component exists in the low field side of plasma [10,11] can be seen with finite poloidal mode numbers. Next, we conducted comparison of the mode spectra in the linear phase ($t = 200$) and nonlinear phase ($t = 400$). In the linear phase, the dominant modes have the poloidal mode numbers of $m = 19$ around $\rho = 0.65$, where the pressure gradient is larger. Here m is the poloidal mode number. On the other hand, in the nonlinear phase, dominant modes exist around $\rho = 0.45$. This is because the pressure profile near $\rho = 0.65$ is flattened by the instabilities, and the steeper gradient region is shifted to the inner part near $\rho = 0.45$. In this way, the mode excited region is expanded in accordance with the flattening process. After the flattening by the ballooning modes, the $n = 1$ mode induces sudden change of the pressure profile in the central region as in Fig. 3 ($t = 500$ and $t = 600$). A $m/n = 1/1$ kink mode at the $q = 1$ surface [12] gives the collapse near the center. In this way, both of ballooning and kink modes are excited in this simulation.

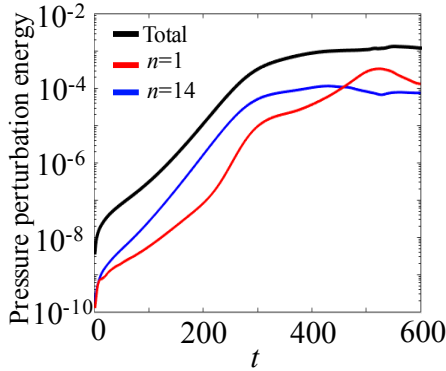


Fig. 2 Time evolutions of the pressure perturbation energy.

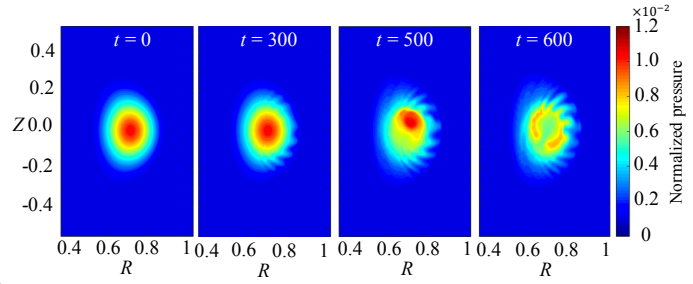


Fig. 3 Time evolution of the pressure profile in the poloidal cross-section.

4. Characteristic of the instabilities

In this section the characteristics of the instabilities are investigated by changing plasma parameters; plasma beta, resistivity and safety factor profile. First, the dependency of the ballooning instability on the plasma beta is explained. The linear growth rate becomes larger, as the plasma beta is increased from 1% to 6%. Therefore, it is revealed that this instability is strengthened by the larger pressure gradient. Next, the dependency on the resistivity is examined. We carry out MHD simulations by changing η from 10^{-8} to 10^{-4} . The linear growth rate becomes larger, as η is increased in the range $\eta > 10^{-6}$. Note that $\eta = 10^{-5}$ is used for the nonlinear simulation in the previous section.

In the MHD simulation in Sec. 3, both the ballooning and kink modes appear. The excited mode can be controlled by changing the q profile. Different q profiles are used as the initial conditions. Figures 4 show comparison of the time evolutions of the pressure profile with different q profiles.

In the Fig.4 (a) with $q_{\text{axis}} = 1.3$, there is no $q = 1$ surface in the plasma, so the kink mode is not excited and the ballooning mode is dominant. When the ballooning mode is dominant, there is no sudden change in the central pressure as in Fig. 4(a). On the other hand, in the Fig.4 (b) with $q_{\text{axis}} = 0.5$, since q_{axis} is smaller than the case with $q_{\text{axis}} = 0.8$, the kink mode is more unstable, which causes sudden change in the central pressure as shown in Fig. 4(b). Therefore, the flattening process of the pressure profile is drastic. It is revealed that the flattening process is changed by dominant instabilities.

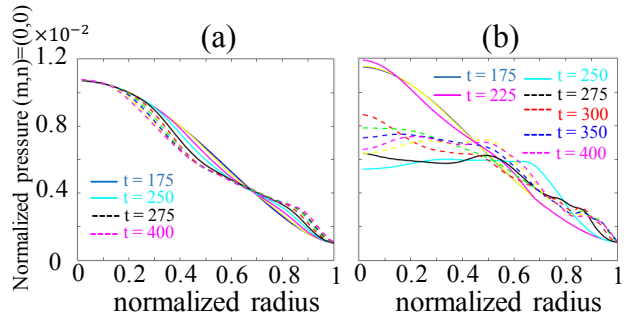


Fig.4 Time evolutions of the pressure profile for the (a) ballooning dominant case ($q_{\text{axis}} = 1.3$) and (b) kink dominant case ($q_{\text{axis}} = 0.5$).

5. Conclusion

In this study, the MHD simulations for PLATO plasmas were carried out by the combination of TASK and MIPS codes. The plasma equilibrium was evaluated with the vertical coil configuration of PLATO by using the free boundary equilibrium code TASK/EQU. The equilibrium was introduced into the MHD simulations and nonlinear saturation dynamics was calculated by using MIPS code. The ballooning and kink modes can both become unstable for the PLATO parameters. The parameter dependencies show their characteristics. The ballooning modes become unstable at the region with steep pressure gradient, which give rather mild flattening of the pressure profile on the low field side of the plasma. On the other hand, the kink modes with $m/n = 1/1$ become unstable near the center of the plasma, and give drastic pressure collapse of the core.

References

- [1] A. M. Dimits, *et al.*, Phys. Rev. Lett. **77**, 1 (1996)
- [2] R. J. Fonck, *et al.*, Phys. Rev. Lett. **70**, 24 (1993)
- [3] K. L. Wong, *et al.*, Phys. Rev. Lett. **85**, 5 (2000)
- [4] Y. Liang, Phys. Rev. Lett. **98**, 265004 (2007)
- [5] P. B. Synder, *et al.*, Phys. Plasmas **9**, 2037 (2002)
- [6] A. Fujisawa, AIP Conf. Proc. **1993**, 020011 (2018)
- [7] <http://bpsu.nucleng.kyoto-u.ac.jp/task/>
- [8] K. Matsuoka, Reports RIAM, Kyushu Univ. **141**, 51 (2011)
- [9] Y. Todo, *et al.*, Plasma Fusion Res. **5**, S2062 (2010)
- [10] J. P. Freidberg, *Ideal MHD* (Cambridge University Press, 2007)
- [11] J. Wesson, *Tokamaks* (Oxford University Press, 2011)
- [12] R. Y. Dagazian and P. H. Rutherford, Phys. Fluids **16**, 1894 (1973)
- [13] M. Yagi, *et al.*, Plasma Fusion Res. **2**, 025 (2007)

Particle transport model in plasma peripheral region

M. Yagi

National Institutes for Quantum and Radiological Science and Technology,
Rokkasho Fusion Institute, Rokkasho, Aomori, Japan

1. Introduction

To understand particle pinch mechanism in the peripheral region of Tokamak is important issue to supply of D-T fuels in DEMO reactor. The inverted density gradient appears in a hollow density profile when gas-puff or pellets are injected. Using a delta-f electromagnetic gyrokinetic simulation code dFEFI[1], we investigated a local dynamics of particle transport in the case with inverted density gradient. It is shown that in the nonlinear phase, the lower wave number mode becomes dominant, which produces an inward particle flux[2]. With a high electron collisionality, electron temperature fluctuations associated with the effects of finite electron thermal conductivity can produce a phase shift between the density and electrostatic potential fluctuations. The phase shift causes an inward pinch in the ITG-like mode, so called ‘ion-mixing mode’[3]. On the other hand, we have also observed that the similar phenomena in the 5-field reduced MHD simulation with density hump where ITG is not taken into account[4]. In this work, we investigate the electron drift wave (EDW) with inverted density gradient. It is shown that in this situation, it could drive inward particle flux rather than the ion-mixing mode.

2. Electron drift wave

The electron response is modeled as

$$\frac{\tilde{n}_e}{n} = \frac{e\tilde{\phi}}{T_e} (1 + i\delta) , \quad (1)$$

with $\delta = k(\omega - \omega_{*e} + 1.5\eta_e\omega_{*e})/\omega_\chi$, $k = 1.76$, $\omega_\chi = k_\parallel^2 v_{the}^2 / \nu_e$. According to Ref.[5,6], we obtain

$$1 + i\delta - \frac{1}{\Omega} + \left(-\frac{k_\parallel^2 c_s^2}{\omega_{*e}^2} \frac{1}{\Omega^2} + b_s + \frac{2\epsilon_n}{\Omega} \right) \left(1 + \frac{K}{\Omega} \right) = 0 . \quad (3)$$

Then, the quartic equation is obtained as

$$i \frac{1}{\hat{\omega}_\chi} \Omega^4 + \left(1 + b_s + i \frac{\hat{\eta}_e}{\hat{\omega}_\chi} \right) \Omega^3 + (-1 + b_s K + 2\epsilon_n) \Omega^2 + (-\xi^2 + G) \Omega - S = 0 , \quad (4)$$

where $G = 2\epsilon_n K$, $\xi = k_\parallel c_s / \omega_{*e}$, $S = K \xi^2$, $\hat{\omega}_\chi = k \omega_\chi / \omega_{*e}$, $\hat{\eta}_e = 3/2 (\eta_e - 2/3)$. G represents the driving term of toroidal ITG mode and S , the one of slab ITG mode.

The particle flux is given by

$$\Gamma = -n_0 \sum_k \left| \frac{e\phi_k}{T_e} \right|^2 \frac{kT_e}{eB} \text{Re}(\delta) . \quad (5)$$

If $\delta > 0$, Eq.(5) implies the inward particle flux. In Eq.(4), we shall consider the electron drift wave with the inverted density gradient, namely, $\omega_{*e} < 0$. Setting $b_s = 0, \xi = 0, G = 0, S = 0, \epsilon_n = 0$, Eq.(4) reduces to the quadratic equation as

$$\Omega^2 + (-i\hat{\omega}_\chi + \hat{\eta}_e)\Omega + i\hat{\omega}_\chi = 0 . \quad (6)$$

In the limit of $|-i\hat{\omega}_\chi + \hat{\eta}_e|^2 \gg 4\hat{\omega}_\chi$, the unstable solution is given by

$$\omega \approx \omega_{*e} - i\frac{3}{2}\left(\omega_{*T_e} - \frac{2}{3}\omega_{*e}\right)\frac{k\omega_{*e}}{\omega_\chi} . \quad (7)$$

Since $\omega_{T_e} > 0$, the imaginary part is positive. Then,

$$\text{Re}(\delta) = \frac{3}{2}k \frac{\omega_{*T_e}}{\omega_\chi} > 0 , \quad (8)$$

which implies the inward particle flux is driven by the electron drift wave with the inverted density gradient. This model is suitable for semi-collisional regime where the passing electron plays a role. On the other hand, if the collision frequency enters the banana regime, the trapped electron may play a similar role.

3. Effect of dissipative trapped electron mode on EDW

We consider the dissipative trapped electron mode (DTEM) on the electron drift wave assuming $\nu_e \sim \omega_b$. The electron response is modeled as

$$\frac{\tilde{n}_e}{n} = \frac{e\tilde{\phi}}{T_e} (1 + i\delta + i\delta_t) . \quad (9)$$

For the DTEM, the nonadiabatic electron response is given by[7]

$$\delta_t \approx \frac{4\sqrt{2}}{\sqrt{\pi}} \frac{\epsilon^{3/2}\omega_{*e}}{\nu_e} \left(\Omega - \left(1 + \frac{3}{2}\eta_e\right) \right) \quad (10)$$

For $\Omega \sim 1$, it is found that the particle flux is the outward, namely,

$$\Gamma = -n_0 \sum_k \left| \frac{e\phi_k}{T_e} \right|^2 \frac{kT_e}{eB} \text{Re}(\delta_t) \approx + \frac{6\sqrt{2}}{\sqrt{\pi}} n_0 \sum_k \left| \frac{e\phi_k}{T_e} \right|^2 \frac{kT_e}{eB} \frac{\epsilon^{3/2}}{\nu_e} \omega_{*T} > 0 . \quad (11)$$

DTEM effect on inverted density gradient driven EDW is easily taken into account of the nonlocal dispersion relation given by Eq.(11) in Ref.[6],

$$(\Omega + \epsilon_n^*)(\Omega - 1)(1 + i\delta_t)^2 - \nu_e^{*2}\Omega(\Omega + \hat{\eta}_e)^2 = 0 . \quad (12)$$

It implies that DTEM has a stabilizing effect on EDW through the factor $1 - \delta_t^2$.

4. Summary and discussion

We investigate the EDW in the case with the inverted density gradient and normal temperature gradient in tokamak plasma peripheral region. The local dispersion relation

Eq.(7) shows the electron temperature gradient and the parallel electron thermal conductivity drives the instability in the case with $\omega_{*e} < 0$ which produces the inward particle flux. We also investigate the effect of DTEM on EDW. It is found that DTEM has a stabilizing effect on EDW through the factor $1 - \delta_t^2$ and weaken the inward particle flux.

To transport the tritium fuel in the core region, we need another mechanism which produces the inward particle flux. The fluid model which describes ITG/TEM turbulence in the collisionless regime was proposed by Nordman et al.[8]. In their paper, they investigated the particle pinch and thermal pinch regime in the phase space of (ϵ_n, η) . There exists the region where the particle pinch occurs. For this region, ITG is unstable and coupled with TEM. The growth rate is given by[8],

$$\gamma = \sqrt{\frac{1 + \sqrt{\epsilon}}{1 - \sqrt{\epsilon}} \left\{ \epsilon_n (1 + \eta) - \frac{7}{4} \epsilon_n^2 \right\} - \frac{(1 - \epsilon_n)^2}{4}}$$

To couple the plasma core with the edge, we shall consider the phase space $(v_e, L_{T_e}, L_n, L_{T_i})$ instead. For future work, we could try the Gedanken experiments, namely, (1) assuming quasi-linear flux, we search the region which gives particle pinch and thermal pinch in parameter space, making phase space map, then, (2) learning steady state profile changing heat source and particle source to approach such region by the neural network, then, we could make particle control by the neural network.

Acknowledgments

The author would like to thank Drs. N. Miyato, A. Matsuyama, N. Kasuya and T. Takizuka for useful comments.

References

- [1] B. Scott, Phys. Plasmas **A17** (2010)102306
- [2] K. Miki, N. Miyato, B. Scott and M. Yagi, 26th International Toki Conference, NIFS, 2017/12
- [3] B. Coppi and C. Spight, Phys. Rev. Lett. 41 (1978) 551
- [4] M. Yagi et al., IAEA FEC 2016, Kyoto (2016) THP3-21.
- [5] F. Romanelli, Phys. Fluids **B 1** (1989) 1018.
- [6] M. Yagi, et al., Proceedings of 16th Burning Plasma Simulation Initiative Meeting, Nov. 29-30, 2018, Kyushu University, Kasuga, Japan.
https://www.riam.kyushu-u.ac.jp/sosei/bpsi/2018/BPSI2018_proc.pdf
- [7] R. Romanelli and S. Briguglio, Phys. Fluids **B 2** (1990) 754.
- [8] H. Nordman et al., Nucl. Fusion 30 (1990) 983.

Study of multiple impurity seeding effect using SONIC integrated divertor code for JT-60SA plasma prediction

Shohei YAMOTO¹⁾, Kazuo HOSHINO²⁾, Tomohide NAKANO¹⁾, Nobuhiko HAYASHI¹⁾

¹⁾QST, ²⁾Keio Univ.

1. Introduction

The JT-60SA tokamak is now being constructed and is expected to ignite the first plasma at 2020 and to perform ITER-supporting and -complementing experiments from 2023 under various operation scenarios. One of the underlying operation scenarios is the high-beta operation under full non-inductive current drive conditions (steady-state high-beta operation) [1]. The operation will take place with impurity seeding to reduce the heat load towards the divertors and with keeping the separatrix density low enough to match the core operation condition. On the other hand, the concentration of the impurities in the core causes a harmful effect to sustain the high-performance plasma by radiation cooling and dilution. Therefore, it is important to establish a method to control the impurity transport in the core and SOL/divertor regions. So far, a favourable spatial distribution of radiation power has been achieved by Ne + Ar (mixed gas) seeding experiment in JT-60U, i.e. the radiated power is almost localized in the divertor region and as a consequence, better energy confinement than Ne-only and Ar-only cases has been achieved [2]. However, the interpretative and predictive simulation of such mixed gas seeding operation has not been performed. This is partly because the number of impurity species that the previous version of integrated divertor plasma transport code SONIC [3,4] could kinetically solve was limited to one. The issue has been essentially resolved by restructuring SONIC code with Multiple-Program Multiple-Data (MPMD) framework [5], which allows SONIC to calculate transport processes of two impurity species by a kinetic impurity transport code IMPMC. The extended SONIC code was applied to the analysis of the JT-60SA divertor plasma with two impurity species, i.e., the intrinsic C and seeded Ar gas impurities, and demonstrated the radiative divertor plasma scenario [5]. The purpose of this paper is to examine the effects of different impurity seeding species in the JT-60SA divertor plasmas step-by-step in order to study the potential impurity seeding operation regime. Aiming for this purpose, the SONIC code has been further extended to handle three or more impurity species kinetically based on the MPMD framework mentioned above. Now the SONIC code is capable of calculating the mixed seeding impurities Ne + Ar and intrinsic C transport by IMPMC. The impurity-impurity interaction such as the physical sputtering of C by Ne and Ar bombardment has been also implemented. The effects of seeding mixture of Ne and Ar in JT-60SA steady-state high-beta operation scenario is demonstrated by means of the extended version of SONIC. The impurity accumulation in the core plasma and its influence on the core plasma are also evaluated by the core integrated code TOPICS using boundary condition of impurity contents in the core edge region evaluated in SONIC, as the same way as in ref. [6]

2. Calculation conditions

Figure 1 shows the computational grid for JT-60SA. The locations of the injection ports of each impurity species are also shown in Fig. 1. The intrinsic C impurities are also considered in the calculation. In this study, the parametric survey of the Ne seeding rate (0.0 (Ar-only) – 0.28 Pa m³/s) is performed with other parameters kept the same as ref. [5] by SONIC. The Ar seeding rate is automatically adjusted to keep the total radiation power to be 13MW in the plasma.

The TOPICS calculation conditions are the same as ref. [6]. The CDBM is employed as the anomalous heat transport model. The same transport coefficients as ref. [6] are employed for the impurity transport calculation in the core.

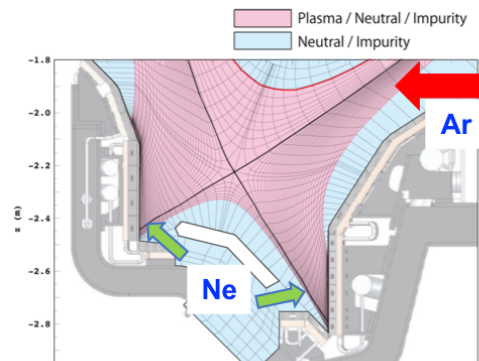


Fig. 1 Computational grid for JT-60SA. The locations of the injection ports of each impurity species are also indicated.

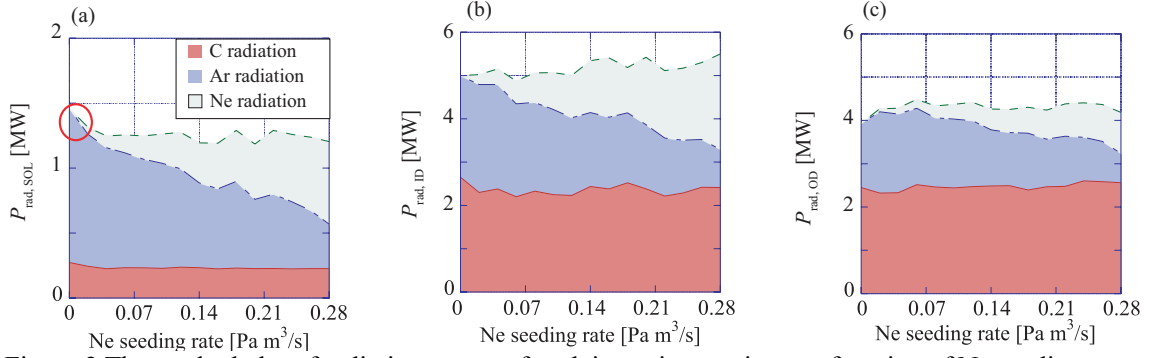


Figure 2 The stacked plot of radiation power of each impurity species as a function of Ne seeding rate: (a) the SOL region above X-point, (b) the inner divertor region, and (c) the outer divertor region.

3. Results

3.1 SONIC calculation

Figure 2 shows the impurity radiation power as a function of Ne seeding rate in (a) SOL region above X-point, $P_{\text{rad, SOL}}$, (b) inner divertor region $P_{\text{rad, ID}}$ and (c) outer divertor region $P_{\text{rad, OD}}$. The rapid decrease of the Ar radiation power from 1.2 MW to 0.9 MW as the Ne seeding rate increases from 0.0 to 0.02 Pa m³/s is due to the change of the balance between the friction force and the thermal force as discussed in ref. [7]. Then, the Ar radiation power in the SOL region gradually decreases as the Ne seeding rate increases. The Ne radiation takes place mainly in the inner divertor region and $P_{\text{rad, ID}}$ increases due to the Ne seeding as seen from Fig. 3 (b). On the other hand, Ne radiation power does not so much increase in the outer divertor region as seen from Fig. 3 (c). In summary, $P_{\text{rad, SOL}}$ decreases and $P_{\text{rad, ID}}$ and $P_{\text{rad, OD}}$ increases. Such compression of impurity radiation power in the mixed-impurity seeding case has also been observed in the JT-60U mixed impurity seeding experiment [2]. The analysis of JT-60U experiment will be performed near future.

3.2 TOPICS calculation

The plasma/impurity transport simulation in the core has been carried out by the TOPICS code using core edge impurity densities computed by the SONIC as a boundary parameter. The following four cases are compared;

- Case A: Ar-only (0.35 Pa m³/s), total radiation 14MW,
- Case B: Ar (0.25 Pa m³/s) + Ne (0.04 Pa m³/s), total radiation 13MW,
- Case C: Ar (0.20 Pa m³/s) + Ne (0.10 Pa m³/s), total radiation 13MW,
- Case D: Ar (0.14 Pa m³/s) + Ne (0.20 Pa m³/s), total radiation 13MW.

It should be noted that the Case A is different from the Ar-only case regarding the total radiation power in Sec. 3.1. The impurity densities $n_{\text{Ar, total}}$ and $n_{\text{Ne, total}}$ at $\rho = 0$, defined as a sum of impurity densities at each charge state, the compression of Ar c_{Ar} , defined as a ratio of the divertor Ar density to the core Ar density, Z_{eff} at $\rho = 0$, the total impurity radiation power in the core ($0 < \rho < 1$), $P_{\text{rad, core}}$, and T_e at $\rho = 0$ are summarized in Table 1. Higher c_{Ar} in Cases B, C and D than Case A has been achieved. The lower Z_{eff} at $\rho = 0$ and $P_{\text{rad, core}}$ than Case A has been achieved in Cases B, C, and D. The higher T_e at $\rho = 0$ than Case A in Cases B, C, and D has also been obtained.

TABLE 1 The summary of the impurity densities $n_{\text{Ar, total}}$ and $n_{\text{Ne, total}}$ at $\rho = 0$, defined as a sum of impurity densities at each charge state, the compression of Ar c_{Ar} , Z_{eff} at $\rho = 0$, the total impurity radiation power in the core ($0 < \rho < 1$) $P_{\text{rad, core}}$, and T_e at $\rho = 0$ in each case

Case	$n_{\text{Ar, total}} (\times 10^{17} \text{ m}^{-3})$	$n_{\text{Ne, total}} (\times 10^{17} \text{ m}^{-3})$	c_{Ar}	Z_{eff}	$P_{\text{rad, core}} (\text{MW})$	$T_e (\text{keV})$
Case A	3.60	-	1.19	3.50	5.83	4.66
Case B	2.31	1.10	3.03	3.10	4.22	4.97
Case C	1.98	2.87	3.45	3.20	4.10	5.01
Case D	1.30	5.35	5.56	3.22	3.64	5.07

4. Summary

The first application of SONIC to the mixed-impurity seeding operation in JT-60SA steady-state high-beta plasma has been carried out to study multiple impurity seeding effect. The parametric survey of Ne seeding rate has been performed. The Ne impurities are injected to the Ar seeded plasma with the Ne seeding rate of 0.0 - 0.28 Pa m³/s. The rapid decrease of the Ar radiation power from 1.2 MW to 0.9 MW as the Ne seeding rate increases from 0.0 to 0.02 Pa m³/s is due to the change of the balance between the friction force and the thermal force as discussed in ref. [7]. Then, the Ar radiation power in the SOL region gradually decreases as the Ne seeding rate increases. The Ne radiation takes place mainly in the inner divertor region and $P_{\text{rad, ID}}$ increases due to the Ne seeding. On the other hand, Ne radiation power does not so much increase in the outer divertor region. These change of radiation power in the SOL suggests that Ne injection into the Ar-seeded plasma has a capability of compressing the Ar impurities into the inner divertor region. Such compression of Ar impurities into the divertor regions results in the higher impurity radiation power in the divertor regions, and lower impurity radiation power in the SOL region in Ar + Ne seeding case, which show the similar tendency observed in JT-60U mixed-impurity seeding experiment [2].

The core plasma has been also investigated by the TOPICS code using the core edge impurity density computed by the SONIC code as a boundary parameter. The Ne injection into the Ar-seeded plasma results in the higher compression ratio of the divertor Ar density to the core Ar density, i.e. the Ar impurities have been compressed in the divertor region in Ar + Ne seeding cases. The Ar + Ne seeding cases show lower Z_{eff} at $\rho = 0$ and total radiation power in the core. The higher T_e than the Ar-only case at $\rho = 0$ has been obtained. These possible contributors to the better energy confinement suggest that the mixed-impurity seeding operation is one of choices in terms of the dilution and radiation in the core plasma.

References

- [1] JT-60SA Research Plan
(http://www.jt60sa.org/pdfs/JT-60SA_Res_Plan.pdf)
- [2] N. Asakura, *et al.*, Nucl. Fusion **49** (2009) 115010.
- [3] H. Kawashima, *et al.*, Plasma Fusion Res. **1** (2006) 031.
- [4] K. Shimizu, *et al.*, Nucl. Fusion **49** (2009) 065028.
- [5] K. Hoshino, *et al.*, Contrib. Plasma Phys. **56** (2018) 638.
- [6] N. Hayashi, *et al.*, Nucl. Fusion **58** (2018) 066001.
- [7] S. Yamoto, *et al.*, Plasma Phys. Control. Fusion, in press.

Stability of di-vacancy and interaction with inevitable impurities in metals

Kazuhito Ohsawa¹, Takeshi Toyama², Yuji Hatano³, Masatake Yamaguchi⁴

¹Research Institute for Applied Mechanics, Kyushu University

²Institute for Materials Research, Tohoku University

³Hydrogen Isotope Research Center, University of Toyama

⁴Center for Computational and e-system, Japan Atomic Energy Agency

1. Introduction

Divertor armor tiles installed in fusion reactors will be exposed to intense plasma particle irradiation. So, the divertor armor tiles are covered by tungsten (W) or its alloys because they have excellent properties as plasma facing materials, e.g., low hydrogen (H) solubility, high melting point, and high mechanical toughness etc. However, a large amount of H isotopes (D and T) retention has been reported in the W materials. In particular, tritium inventory is an important subject associated with the safety of the fusion reactors. Vacancy-type lattice defects are important trapping sites for H isotopes. So, the stability and binding energy of vacancy cluster with H isotopes are investigated in some previous works [1,2]. Besides, some abnormal properties have been reported associated with vacancy clusters in the W specimen. As an example, di-vacancy in W is energetically unstable, according to first-principle calculations. So, small vacancy clusters were also expected to be unstable. However, the vacancy cluster growth from mono-vacancy was observed by positron annihilation lifetime spectroscopy which is sensitive experiment for observation of such vacancy-type lattice defects in metals. In the present work, we propose a solution to resolve the contradiction between the simulation and experiment. Some kinds of inevitable impurities, carbon (C), nitrogen (N), and Oxygen (O) are contained in the W materials. The vacancy clusters are remarkably stabilized by the impurities. In particular, stabilization due to the presence O is extensively investigated.

2. Methodology

Stable structures of vacancy-type lattice defects in W and their binding energies are estimated in terms of first-principle calculations on the basis of density functional theory. The simulations are performed by using Vienna ab-initio simulation package (VASP) with PBE type potential. The cut-off energy of plane wave is 520eV. We use large supercell composed of 432 lattice points ($6 \times 6 \times 6$ BCC lattice) in the present calculations in order to reduce the effects of periodic boundary condition imposed on the supercell. Lattice relaxations are iterated until resultant force of each atom is lowered than 0.003 eV/Å.

The binding energies E_b of the vacancy-type lattice defects are calculated, as bellows.

$$E_b = E[\text{reactants}] - E[\text{products}], \quad (1)$$

where E is the cohesive energy of the supercell. As an example, binding energy of vacancy and vacancy-impurity complex is expressed as

$$E_b = E[\text{W}_{n-1}\text{V}] + E[\text{W}_{n-1}\text{VX}] - E[\text{W}_{n-2}\text{V}_2\text{X}] - E[\text{W}_n], \quad (2)$$

where V and V₂ mean mono-vacancy and di-vacancy, respectively. Impurities are denoted by X. The total number of lattice points for W atoms is $n=432$. Positive and negative binding energies correspond to attractive and repulsive interaction, respectively.

The migration energies for the impurities and mono-vacancy in the bulk W are estimated by nudged elastic band method which is established scheme to calculate activation energy.

3. Results

We investigated two types of di-vacancy, first nearest neighbor (1nn) and second nearest neighbor (2nn) configurations, as shown in Fig. 1. Impurities in the bulk W are located close to octahedral interstitial sites (O-sites) next to the di-vacancy. The binding energies of di-vacancy with and without impurities are summarized in Table I. The intrinsic di-vacancy without impurities in the bulk W is unstable, which is good agreement with previous works [1-2]. In particular, strong repulsion is observed at the di-vacancy in the 2nn configuration. On the contrary, the di-vacancy is remarkably stabilized by impurities occupying an appropriate O-site. The most stable structure of di-vacancy is the 2nn configuration and impurities are located at O-site ③, according to Table I. All impurities contribute the stabilization but the effect of H is small, compared with other impurities (C, N, and O).

Fig. 2 shows barrier height for each impurity and mono-vacancy along the migration path in bulk W. The migration energy for O is very small, compared with other impurities. So, O is expected to quickly diffuse in the bulk W and be trapped in a mono-vacancy at low temperature. Therefore, we extensively investigate the effect of O for the stabilization in the present work.

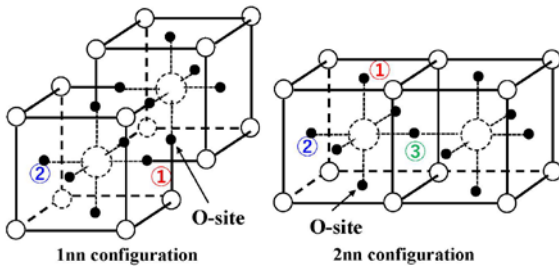


Fig. 1: Schematic view of di-vacancy in 1nn and 2nn configurations in BCC lattice. Symbols ①, ②, and ③ indicate O-sites next to the di-vacancy which are favourable positions for impurity in di-vacancy.

1nn configuration			2nn configuration			
	①	②		②	③	
C	-0.4014	-0.0383	C	-0.1548	-0.4565	1.0923
N	0.1126	-0.0637	N	-0.1361	-0.4400	1.1425
O	0.7218	-0.0808	O	-0.0098	-0.4399	1.3860
H	0.1006	-0.1183	H	-0.4427	-0.3394	0.1693
V	V+V→V ₂	-0.1260	V	V+V→V ₂	-0.4546	

Table I: Binding energies of di-vacancy (eV) estimated in Eq. (2). C, N, O, and H denote impurities and the lowest row V corresponds to intrinsic vacancy without impurities. Symbols ①, ②, and ③ indicate O-sites represented in Fig. 1.

We estimate binding energies for vacancy clusters composed of six or less than six mono-vacancies with and without O referring to Eq. (1), as shown in Fig. 3. Small vacancy clusters without O trapping, V_2 and V_3 , are supposed to be unstable because of the negative binding energies. However, vacancy clusters without O composed of four or more than four mono-vacancies are stable. On the other hand, the vacancy clusters are extremely stabilized by O trapping.

4. Summary and discussion

The di-vacancy in the bulk W was expected to be unstable, according to first-principle calculations but vacancy-cluster growth was observed in positron annihilation lifetime spectroscopy. We focus on the inevitable impurities in W specimen and investigated the stabilization effects by the impurities. The vacancy clusters are considerably stabilized by the impurities (C, N, O, and H). Among them, O is expected to play the most effective role for the stabilization due to its large diffusivity.

Acknowledgement

This work was supported by JSPS KAKENHI Grant Number JP17K06993 and Computational Simulation Center of International Fusion Energy Research Center (IFERC-CSC), Aomori, Japan in National Institutes for Quantum and Radiological Science and Technology.

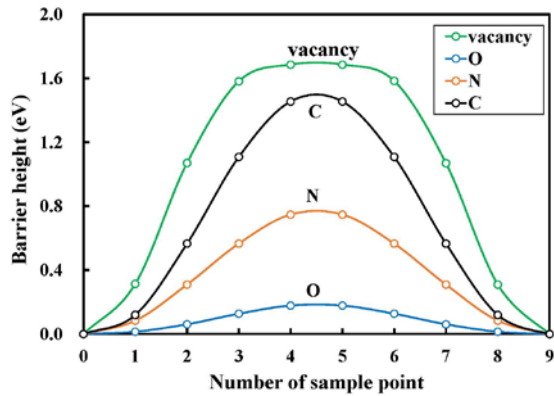


Fig. 2: Barrier height for impurities and mono-vacancy along migration path (eV).

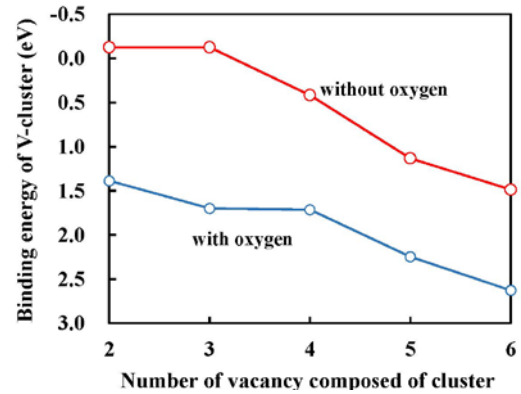


Fig. 3: Binding energies for vacancy clusters with and without O (eV).

References

- [1] L. Ventelon *et al.*, J. Nucl. Mater. 425 (2012) 16.
- [2] K. Ohsawa *et al.*, J. Nucl. Mater. 527 (2019) 151825.

Tungsten transport analysis using integrated code TASK

I. Shimomura¹, N. Kasuya^{1,2}, A. Fukuyama³, S. Mochinaga¹ and M. Yagi⁴

IGSES, Kyushu Univ.¹, RIAM, Kyushu Univ.², Kyoto Univ.³, QST⁴

Introduction

One of the problems for maintaining high-temperature plasmas is that impurities generated from the wall of the reactor flow into the core plasma. Since confined energy is lost by emission from impurities, the inflow of impurities makes plasma temperature lower. In ITER [1] and the next-generation fusion reactor, usage of materials with high melting point, high thermal conductivity, and high charge number, such as tungsten, is planned [2]. Since the effect of the impurities is serious, it is necessary to control its flow and accumulation appropriately.

In this research, code development of an integrated transport simulation is carried out to establish control scenario of impurities in core plasmas of fusion devices. The transport calculation routine including the transport process and atomic process of tungsten is implemented in TASK [3] integrated transport simulation code, which enables evaluation of impurity transport processes and its response to plasma heating.

NCLASS (neoclassical transport model)

NCLASS [4] is a code for calculating neoclassical transport properties of axisymmetric plasmas of arbitrary aspect ratio and geometry. By giving temperature and density profiles of electron and ion as input parameters, the coefficients for the neoclassical particle flux of impurity ion in the following equation are calculated;

$$\Gamma_k^{neoc} = -D_k \frac{\partial n_k}{\partial \rho} + D_k n_k \left[\sum_{l \neq k} \left(g_l \frac{\partial n_l}{\partial \rho} \right) + g_{T_i} \frac{\partial T_i}{\partial \rho} \right]. \quad (1)$$

The temperatures of impurities are assumed to be equal to that of bulk ions. These coefficients are introduced into the transport code.

Atomic process database OPEN-ADAS

The TASK code is developed to include a library for ADAS database [5] for atomic processes such as ionization and recombination. Figure 1 shows the charge number dependence of the difference between the ionization and recombination coefficients of

tungsten obtained from the OPEN-ADAS database. Using these data, time evolution of the impurities is solved.

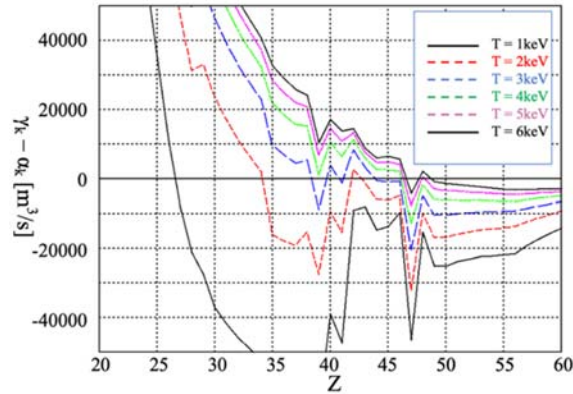


Fig. 1 Charge number dependence of ionization and recombination rates.

Simulation results

Using the TASK / TR and TI transport modules, radial profiles of the density of bulk ions, electrons and impurities in the steady state are evaluated. Here TR and TI are modules for bulk plasmas and impurities, respectively. Figure 2 shows an example of radial profiles of the convective velocity of bulk plasma and tungsten ions. The particles have negative convective velocities, which corresponds to existence of inward pinch, in this case.

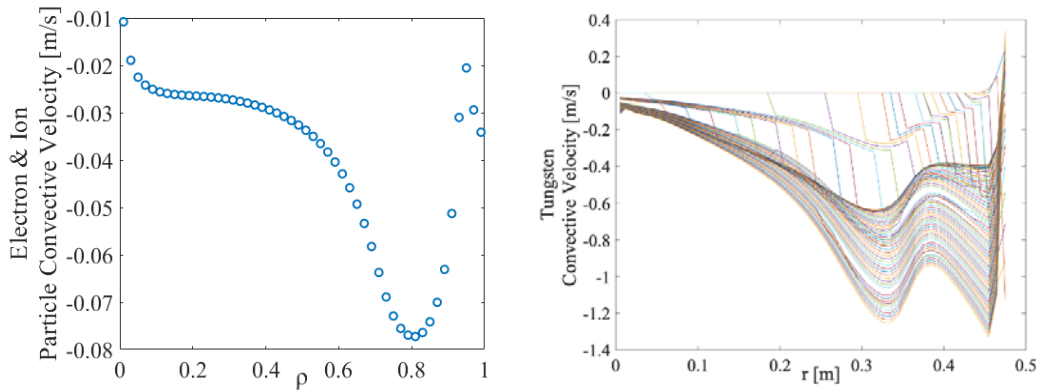


Fig. 2 Radial profiles of the convective velocity of bulk plasma (left) and tungsten ions (right).

Radial profiles of the tungsten density are evaluated with fixed bulk plasma profiles using TASK / TI module (Fig. 3). Tungsten flowing into the plasma from the boundary is transported to the core accompanied with repeated ionization and recombination. The density accumulation of highly charged ions is enhanced by the pinch effect. Figure 4 evaluates the density peaking of the impurity by the particle pinch. As shown in Fig. 4,

the higher the inward convection velocity is, the stronger the density accumulation becomes. This dependency is evaluated with constant convective velocities in space to show the necessary magnitude of convection for density accumulation.

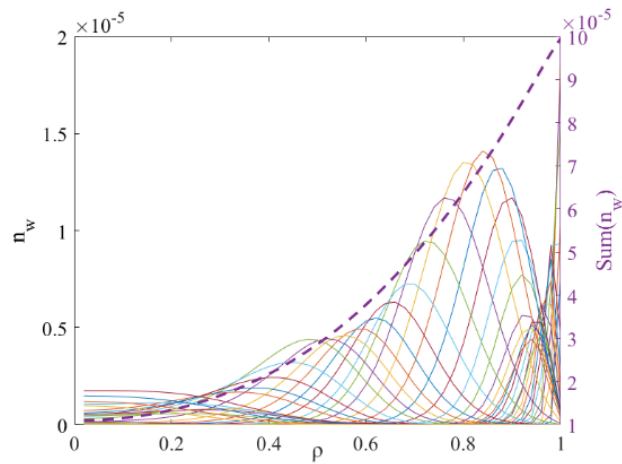


Fig. 3 Radial profile of tungsten ions.

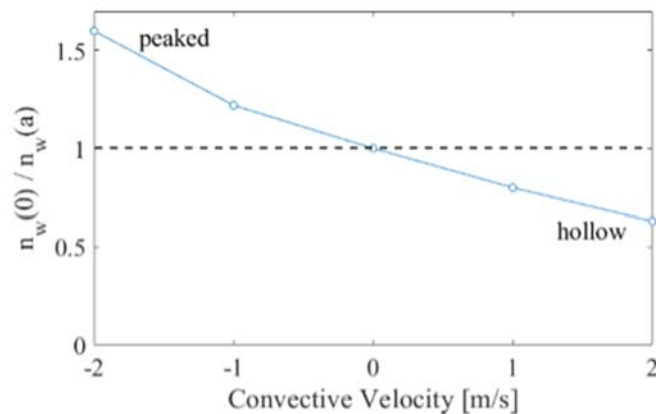


Fig. 4 Dependence of density accumulation on the pinch velocity.

References

- [1] ITER Organization website, <https://www.iter.org/>
- [2] R.A. Pitts, *et al.*, J. Nucl. Mater. **438** (2013) S48.
- [3] TASK code website, <http://bpsu.nucleng.kyoto-u.ac.jp/task/>
- [4] W. Houlberg, *et al.*, Phys. Plasmas **4** (1997) 3230.
- [5] ADAS website, <http://www.adas.ac.uk/>

統合輸送シミュレーションスキームを用いた実験室プラズマの解析

Analysis of laboratory torus plasma using the integrated simulation scheme

N. Kasuya ^{1,2}, I. Shimomura ², S. Tomimatsu ², S. Mochinaga ², A. Fukuyama ³, M. Yagi ⁴, Y. Nagashima ^{1,2} and A. Fujisawa ^{1,2}

¹ Research Institute for Applied Mechanics, Kyushu University, Kasuga, Fukuoka 816-8580, Japan

² Interdisciplinary Graduate School of Engineering Sciences, Kyushu University, Kasuga, Fukuoka 816-8580, Japan

³ Kyoto University, Nishikyo-ku, Kyoto 615-8540, Japan

⁴ National Institute for Quantum and Radiological Science and Technology, Obuchi, Rokkasho, Aomori 039-3212, Japan

E-mail: kasuya@riam.kyushu-u.ac.jp

PLASMA Turbulence Observatory (PLATO) is a torus device, which is now being under construction in Kyushu university [1]. The aim of the research project is to deepen understanding of plasma turbulence phenomena by measuring spatio-temporal structures of plasma fluctuations in this device with various high resolution diagnostics. For prediction and interpretation of plasma phenomena in PLATO, we are carrying out simulation researches by using various modules in TASK code [2]. TASK code is an integrated code to calculate self-consistent states of burning plasmas by combining several modules for physical processes in plasma core and peripheral regions. Communication between the modules is possible with interfaces for the common data set. Figure 1 shows the schematic of module configuration in TASK used in this research. EQ module is to calculate plasma equilibrium with a fixed boundary condition. TR module is to calculate profiles of bulk plasmas considering neoclassical and anomalous transport processes. TI module is developing in this research to calculate profiles of impurity ions considering atomic processes between various charge states [3]. WR module calculate RF wave propagation, so can evaluate power deposition by ECH in tokamak. In addition to the prepared function, extension is being made to simulate experimental diagnostics for direct comparison between simulations and experiments.

As the application of prepared functions of TASK, evaluation of equilibria and transport analyses in PLATO are carried out. Figure 2 shows an example of the equilibrium with considering the external coil configuration in PLATO. This is the case with toroidal magnetic field $B_t = 0.2$ T, plasma current $I_p = 40$ kA, central beta $\beta_0 = 0.6$ %. By changing the plasma current and external coil currents, the corresponding safety factor q profiles and plasma shapes are calculated, such as low central q case and low triangularity case. one-dimensional transport analysis using TR module shows central ion temperature 50 eV and electron temperature 200eV in the case with central electron density $1 \times 10^{19} \text{ m}^{-3}$ sustained by particle supply in the edge region. The information is also used for inputs to other codes. Global simulations of MHD instability and micro instability in real magnetic field geometry are effective to capture 3-D feature of plasma perturbations. MHD simulations are carried out by MIPS code where equilibrium profiles are introduced from TASK/EQ module. Nonlinear saturation dynamics are represented with coexistence of ballooning and kink instabilities [4].

For the new application of the integrated code, experimental diagnostics are simulated numerically. We have been carrying out simulations of turbulence diagnostics in experimental

devices [5]. Perturbation field that is the target for the numerical diagnostics is calculated using reduced MHD model in the equilibrium from TASK/EQ. Three heavy ion beam probes (HIBPs) [6] are planned to observe spatio-temporal patterns of the potential and density fluctuations inside the PLATO plasma, and their measurements are simulated (Fig. 3). For HIBP simulation, not only the static configuration of the plasma device including the equilibrium but also dynamics of plasma turbulence are taken into account. Three-dimensional time-series data from a four-field reduced MHD model [7] are used for the numerical diagnostic. Nonlinear couplings between MHD modes as tearing instability and drift wave modes, which have different spatial scales, can be calculated. The developed code is flexible to apply to other three-dimensional turbulence simulations and device configurations. Microwave reflectometry is also simulated by using TASK/WR module.

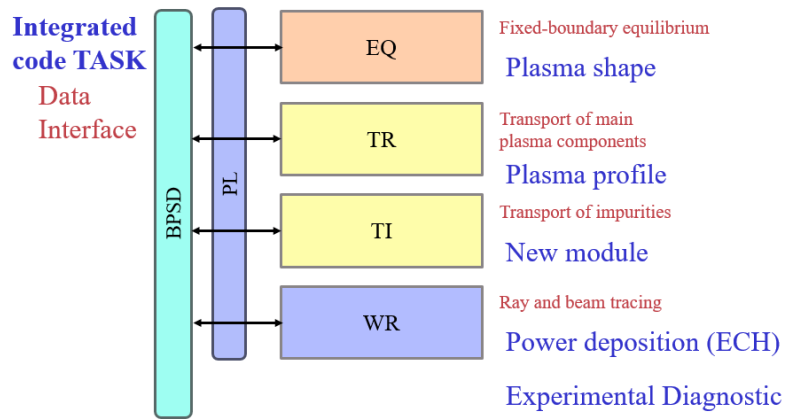


Fig. 1: Schematic of module configuration in TASK integrated simulation code used in this research.

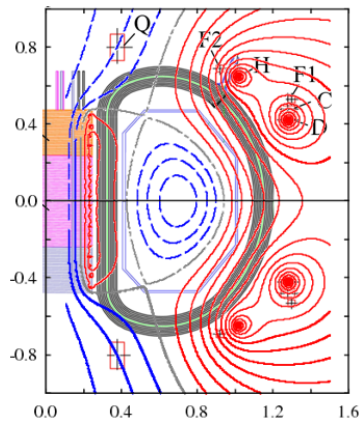


Fig. 2: Equilibrium in PLATO calculated by TASK/EQU module. The positions of the vertical field coils are also indicated.

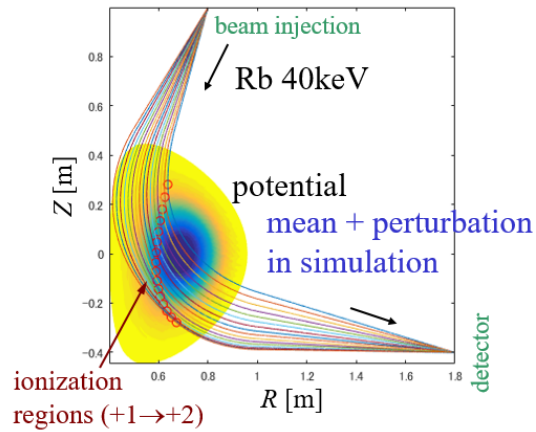


Fig. 3: Trajectory of injected heavy ions in HIBP measurement.

Acknowledgements

This work was partly supported by JSPS KAKENHI Grant Number (JP16K06938, 17H06089), by the collaboration program of NIFS (NIFS19KNST144, NIFS18KNXN373) and RIAM of Kyushu University. JFRS-1 supercomputer in IFERC-CSC and Plasma Simulator in NIFS were used for the nonlinear calculations.

References

- [1] A. Fujisawa, AIP Conf. Proc. **1993** (2018) 020011.
- [2] <http://bpsi.nucleng.kyoto-u.ac.jp/task/>
- [3] I. Shimomura, et al., this meeting, 2-6.
- [4] S. Tomimatsu, et al., this meeting, 2-2.
- [5] N. Kasuya, et al., Plasma Sci. Tech. **13** (2011) 326.
- [6] T. Ido, et al., Rev. Sci. Instrum. **77** (2006) 10F523.
- [7] M. Yagi, et al., Plasma Fusion Res. **2** (2007) 025.

Development of transport prediction scheme based on first-principle simulation and machine learning

Masanori Nunami

National Institute for Fusion Science, Toki 509-5292, Japan

Based on the first-principle gyrokinetic simulations, the machine-learning techniques, and the reduced transport model, a new numerical scheme to predict the plasma turbulent transport levels and the plasma profiles is developed. In the developed scheme, we apply the machine-learning method to find the relevant input parameters of the nonlinear gyrokinetic simulations which should be performed via the reduced transport model, and to optimized the reduced transport model. Using the optimized reduced model obtained from the developed scheme, we can predict the turbulent transport fluxes by first-principle simulations as few times as possible.

1 Introduction

To predict the turbulent transport, the first-principle simulation based on the gyrokinetics is reliable way. Indeed, it becomes possible to validate the gyrokinetic simulation results against the experimental observations for the plasma temperature and density profiles with the experimental errors taken into account[1]. In the validation analyses, by performing gyrokinetic simulations with changing the input parameters about the profiles of the plasma temperature and density, we should find the transport fluxes that agree with the fluxes from the experimental observation. In such validation scheme, which is called “flux-matching technique[2],” we can predict the transport levels or the plasma profiles, quantitatively. However, to obtain quantitatively matched transport flux with the experimental results, numerous gyrokinetic simulation runs should be demanded. In particular, for the case of multi-species plasmas, we must perform a huge number of the simulations to find the matched fluxes in the huge multi-dimensional parameter spaces. On the other hand, the reduced transport model, which is based on the nonlinear simulation results or the data analyses via the machine-learning techniques, enables us to obtain the turbulent transport fluxes without additional heavy gyrokinetic simulations. However, since such reduced models contain finite errors to evaluate the transport fluxes in principle, it is hard to predict the turbulent transport fluxes precisely.

2 Developed scheme

The developed new scheme to predict the turbulent transport is proceeded as follows. In order to reduce the number of the gyrokinetic runs, we have to find the relevant input parameters of the simulations to be able to realize the transport fluxes which is close to the experimental observations. Therefore, first, for finding the input parameters when the nonlinear gyrokinetic simulation should be performed, we employ the reduced ion heat transport model[3] including the turbulent contribution \mathcal{L} and the zonal-flow contribution τ_{ZF} as represented by

$$\frac{\chi_i^{\text{model}}}{\chi_i^{\text{GB}}} = \frac{A_1 \mathcal{L}^{\alpha_0}}{(A_2 + \tau_{ZF}/\mathcal{L}^{1/2})},$$

where, $\mathcal{L} \equiv a(\rho)[R/L_{T_i} - \beta_0 R/L_{T_i}^{\text{cr}}]$ with the critical temperature gradient $R/L_{T_i}^{\text{cr}}(\rho)$ obtained by the linear stability analyses, τ_{ZF} is the normalized zonal-flow decay time estimated by the linear gyrokinetic calculation, $a(\rho)$ is determined from the linear stability analyses, and A_1 , A_2 , α_0 , and β_0 are constant numbers in the model. Using one of the optimization methods in the machine-learning numerical library[4], the flux-matching is performed in the model to guess the initial temperature gradient which realizes the transport flux that agree with the observations in the target plasma. Next, at the guessed temperature gradient as an input parameter, one run of the nonlinear gyrokinetic simulation is performed at each radial position. At last, using the results of the nonlinear runs, the machine-learning is performed again to optimize the reduced model by optimizing the parameters, α_0 and β_0 to α and β , respectively. Then we can obtain the optimized reduced transport model suitable for the target plasma by only one gyrokinetic simulation at each radial position.

3 Prediction by the developed scheme

Figure 1 shows the comparison of the temperature gradient dependences of the ion heat diffusivities obtained by the optimized reduced model, the initial reduced model, and the nonlinear gyrokinetic simulations by using GKV code[5] in the case of the ion temperature gradient driven turbulent transport in the LHD[6]. While the initial reduced model does not agree with the nonlinear simulation results, the results of the optimized reduced model with $\alpha/\alpha_0 = 0.89$ and $\beta/\beta_0 = 0.92$, which are determined by the machine-learning, are quite agree with the nonlinear runs around marginal temperature gradients. If the flux-matching is performed using the optimized model, we can obtain the matched transport flux or the matched heat diffusivities. In the results of χ_i by the flux-matching technique, the turbulent ion heat diffusivities obtained by optimized model can reproduce the original nonlinear simulation results. On the other hand, the initial model cannot reproduce the nonlinear results because the finite errors that essentially exists in the initial reduced model. At least in this case, we can obtain the turbulent transport fluxes which quantitatively agree with the experimental results by using the developed scheme with just once nonlinear simulation at each radial position.

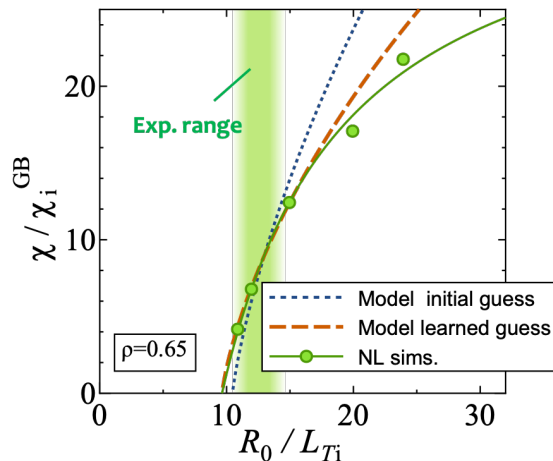


Fig. 1 Comparison of the temperature gradient dependences of the ion heat diffusivities obtained from the optimized model (orange dashed curve), the nonlinear first-principle simulations (green circles), and the initial reduced model (blue dotted curve) at $\rho = 0.65$ in the high- T_i LHD plasma. The green colored region represents the experimentally allowable region of the temperature gradient.

4 Summary

The scheme to predict the turbulent transport fluxes is newly developed. We employ the machine-learning to find the relevant input parameters of the nonlinear gyrokinetic simulations which should be done. By performing just once first-principle simulation with the guessed input parameters for each radial position, the optimized transport model suitable for the target plasma can be obtained. Since the developed scheme enables us to drastically reduce the numbers of the nonlinear simulations, the optimized model can be applied to an integrated transport code.

Acknowledgment

This work is supported in part by the RIAM collaborative Research Program (2019FP-14), JSPS KAKENHI (18H01202, 19H01879 and 19K03801), NIFS Collaborative Research Program (KNST145, KNTT045 and KNTT050), and by FLAGSHIP2020, MEXT within the priority study 6. The results were obtained by using JFRS-1 at IFERC CSC (KML3D and GDKTHEL), and "Plasma Simulator" at NIFS.

- [1] M. Nunami, *et al.*, Phys. Plasmas **25**, 082504 (2018).
- [2] T. Görler, *et al.*, Phys. Plasmas **21**, 122307 (2014).
- [3] S. Toda, *et al.*, J. Phys. Conf. Ser. **561**, 012020 (2014).
- [4] M. Abadi, *et al.*, arXiv:1603.04467 (2016).
- [5] T.-H. Watanabe and H. Sugama, Nucl. Fusion **46**, 24 (2006).
- [6] Y. Takeiri, *et al.*, Nucl. Fusion **57**, 102023 (2017).

Neural-network-based multi-channel turbulent transport modeling

E. Narita¹, M. Honda¹, M. Nakata^{2,3}, M. Yoshida¹ and N. Hayashi¹

¹National Institutes for Quantum and Radiological Science and Technology, Naka, Ibaraki 311-0193, Japan

²National Institute for Fusion Science, Toki, Gifu 509-5292, Japan

³The Graduate University for Advanced Studies, Toki, Gifu 509-5292, Japan

1 Introduction

Since density and temperature profiles severely affect fusion power, understanding and predicting profile formation mechanisms are helpful to obtain high-performance fusion plasmas. A variety of profile shapes has been found in experiments, and we have tried to predict them with several transport models. While theory-based turbulent transport models, such as TGLF [1], show reasonable agreement with experiments, the existing models are hard to use to investigate the relationship between profile formation and transport processes because they do not tell us the breakdown of the calculated particle and heat fluxes. Furthermore, introducing the detailed descriptions of turbulence physics to the transport models tends to increase the computational cost. To resolve the issues, we have developed the turbulent transport model DeKANIS.

2 Prediction of particle and heat fluxes consistent with the quasilinear transport matrix

DeKANIS has originally been developed for particle transport [2], and the capability has been extended to cover both particle and heat transport, predicting turbulent particle and heat fluxes for electrons in a quasilinear limit as $\bar{\Gamma}_e = \bar{D}(R/L_{n_e} + C_T R/L_{T_e} + C_P)$ and $\bar{Q}_e = \bar{\chi}_e(R/L_{T_e} + C_N R/L_{n_e} + C_{HP})$, respectively. Here, non-dimensional \bar{D} , $\bar{\chi}$, R/L_n and R/L_T are the particle and heat diffusivities in proportion to fluctuation amplitudes and the density and temperature gradients, respectively. The fluxes are composed of the diagonal (diffusion) and off-diagonal (pinch) terms, which are quantitatively determined by calculating the off-diagonal-term coefficients (C_T , C_P , C_N and C_{HP}) and the diffusivities (\bar{D} and $\bar{\chi}$). DeKANIS estimates the off-diagonal-term coefficients and the diffusivities with a neural network (NN) model, which is one of the machine-learning techniques, for the speed-up.

The training dataset for the NN construction has been developed with 23 JT-60U ELMy H-mode plasmas. The plasma current and the toroidal magnetic field are $I_P = 1$ MA and $B_\phi = 2.0$ – 2.2 T, respectively, and the plasmas are heated by neutral beams (NBs) whose power is $P_{NB} = 8.9$ – 14.7 MW, without gas puffing. Plasma parameters in $0.3 \leq \rho \leq 0.6$ are used for development of the training dataset, where ρ is the normalized minor radius. The off-diagonal-term coefficients in the training dataset have been given by linear calculations of the local flux-tube gyrokinetic code GKW [3]. As for the particle diffusivity, two different saturation rules of fluctuation amplitudes are applied as shown in section 3: a semi-empirical saturation rule

and a mixing-length-like one. Since the remaining heat diffusivity is intrinsically determined to satisfy the Onsager symmetry between the off-diagonal terms of the particle and heat fluxes, we require the NN model that predicts the off-diagonal-term coefficients and the particle diffusivity.

3 Two different saturation rules of fluctuation amplitudes

The first saturation rule uses experimental turbulent particle fluxes $\bar{\Gamma}_{e,\text{exp}}$, which are estimated on the assumption that the external particle source flux from the NB injection is balanced with the neoclassical particle flux and the turbulent one. The particle diffusivity has been calculated to match $\bar{\Gamma}_{e,\text{exp}}$ in conjunction with $C_{T,P}$ calculated by GKW and $R/L_{n_e,T_e}$ estimated by measurements. The resultant particle diffusivities are used as the training data with the off-diagonal-term coefficients. The NN model has been constructed to reproduce the training dataset, and the heat diffusivity is determined not to break the Onsager symmetry. We note that the saturation level of the fluctuation amplitude is estimated based on $\bar{\Gamma}_{e,\text{exp}}$, without the use of the experimental heat flux $\bar{Q}_{e,\text{exp}}$. The semi-empirical transport model is referred to as DeKANIS-1. Figure 1 demonstrates that DeKANIS-1 gives radial profiles of diagonal and off-diagonal terms individually, and the total particle and heat fluxes are quite close to the experimental ones as shown in figure 2.

The second saturation rule is based on the mixing-length theory. In this paper, the following scaling formula [4] is used: $\bar{D} = 1.86 \times 10^{-4} (\bar{\gamma}/\bar{k}_\theta^2)^{1.5} L_{ZF}^{-2.71}$, where $\bar{\gamma}$ and \bar{k}_θ are the normalized local maximum linear growth rate and the poloidal wavenumber corresponding to $\bar{\gamma}$, and L_{ZF} is the residual zonal flow level. Here, L_{ZF} is given as the product of linear zonal flow response function K_{RH} and the zonal flow potential, which is assumed to be proportional to a square root of $\bar{\gamma}/\bar{k}_\theta^2$ [5], where $K_{RH} = 1/(1 + 1.6q^2/\epsilon^{1/2})$ [6], and q and ϵ are the safety factor and the inverse aspect ratio, respectively. To apply the scaling formula, the other NN model has been constructed to reproduce $\bar{\gamma}$ and \bar{k}_θ that are given by the linear calculations. This theory-based model is referred to as DeKANIS-2. As shown in figure 2, DeKANIS-1 and -2 reproduce the particle and heat

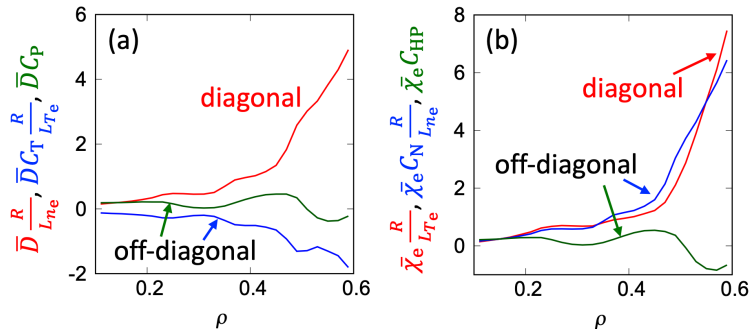


Figure 1. Radial profiles of decomposed (a) particle and (b) heat fluxes predicted by DeKANIS-1 for a plasma outside the NN training dataset.

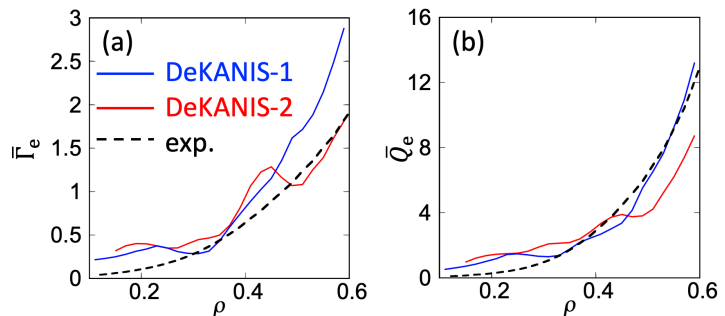


Figure 2. Radial profiles of (a) particle and (b) heat fluxes predicted by DeKANIS-1 and -2 for the same test plasma as in figure 1.

As shown in figure 2, DeKANIS-1 and -2 reproduce the particle and heat

fluxes to a similar degree.

4 Checks of the model accuracy

Both transport models give fluxes in $\sim 10^{-3}$ second with a single CPU, which run $10^3 \sim 10^4$ times faster than the conventionally-used transport models, and they have been validated, using 14 JT-60U ELMy H-mode plasmas as test data. Here, the test data consists of 13 low- I_P plasmas with $I_P = 1$ MA and $B_\phi = 1.9\text{--}2.2$ T, which are close to those of the training dataset and one high- I_P plasma with $I_P = 1.15$ MA and $B_\phi = 2.6$ T.

DeKANIS-1 and -2 have been used to predict particle and heat fluxes of the training and test data. Here, TGLF has also been performed for comparison. For each plasma, mean standard deviations \mathcal{S} for the particle and heat fluxes have been estimated. In figure 3, one can see that $\mathcal{S}_{\bar{\Gamma}_e, \bar{Q}_e}$ of the two models distributes in a similar range between the training and test data, and both DeKANIS versions have the higher accuracy than TGLF.

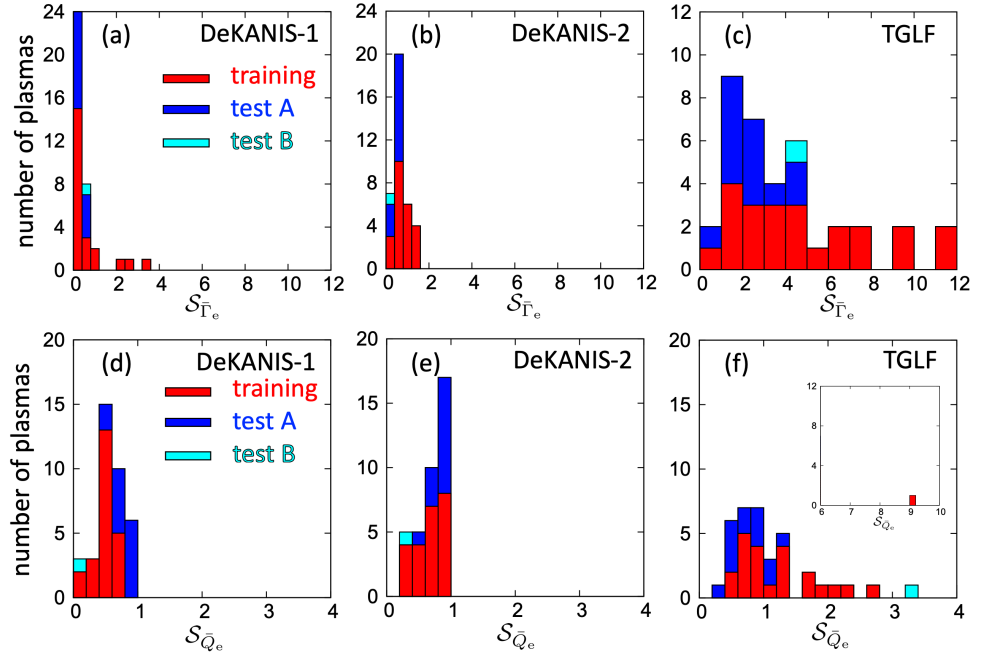


Figure 3. Histograms of the mean standard deviations \mathcal{S} of the (a)–(c) particle and (d)–(f) heat fluxes predicted by (a), (d) DeKANIS-1, (b), (e) DeKANIS-2 and (c), (f) TGLF for the 23 plasmas applied to training the NNs (training, shown by red bars) and the 14 plasmas outside the training dataset (test, shown in blue and cyan). \mathcal{S} for ξ is given as

$$\mathcal{S} = \sqrt{\left(\sum_{\rho} (\xi_{\text{sim}}(\rho) - \xi_{\text{exp}}(\rho))^2\right) / \left(\sum_{\rho} \xi_{\text{exp}}^2(\rho)\right)}, \text{ where } \xi_{\text{sim}(\text{exp})} \text{ is the simulated (experimental) value of } \xi.$$

References

- [1] G.M. Staebler *et al.*, Phys. Plasmas **12** 102508 (2005).
- [2] E. Narita *et al.*, Nucl. Fusion **59** 106018 (2019).
- [3] A.G. Peeters *et al.*, Comput. Phys. Commun. **180** 2650 (2009).
- [4] E. Narita *et al.*, Plasma Phys. Controlled Fusion **60** 025027 (2018).
- [5] M. Nunami *et al.*, Phys. Plasmas **20** 092307 (2013).
- [6] H. Sugama *et al.*, Phys. Plasmas **13** 012501 (2006).

Data assimilation system based on integrated transport simulation of LHD plasma

Y. Morishita¹, S. Murakami¹, M. Yokoyama^{2,4}, G. Ueno^{3,4}

¹Department of Nuclear Engineering, Kyoto University, Nishikyo, Kyoto, 615-8540, Japan

²National Institute for Fusion Science, National Institutes of Natural Science, Toki 509-5292, Japan

³The Institute of Statistical Mathematics, Research Organization of Information and Systems, Tokyo 190-8562, Japan

⁴The Graduate University for Advanced Studies, SOKENDAI, Toki 509-5292 and Tokyo 190-8562, Japan

1. Introduction

Integrated simulation for fusion plasmas has various uncertainties in each of the employed simulation models, specifically turbulent transport model. Because of this, the simulation results also have uncertainties and we can not evaluate the employed simulation models. To solve this problem, data assimilation techniques are applied to the integrated transport simulation by TASK3D [1] for a plasma in LHD.

The purpose of this study is to develop a numerical system that can predict the behavior of fusion plasmas with high accuracy employing the data assimilation. Data assimilation can also improve simulation models involving turbulence models. As data assimilation methods, We use the ensemble Kalman filter (EnKF) [2] to predict the behavior of fusion plasmas with high accuracy and the ensemble Kalman smoother (EnKS) [2] to estimate the models which can reproduce experimental data. The EnKS optimizes the state variables using both past and future data, while the EnKF using only past data.

2. Data assimilation system

In TASK3D, one dimensional (1D) diffusive transport equation is solved. As a turbulent transport model for the LHD plasma, the gyro-Bohm model for electron and the gyro-Bohm gradT model for ion are employed based on previous TASK3D simulations as Eq. 1 and 2.

$$\chi_e^{\text{TB}} = C_e \frac{T_e}{eB} \frac{\rho_i}{a} \quad (1)$$

$$\chi_i^{\text{TB}} = C_i \frac{T_i}{eB} \frac{\rho_i}{a} \left(\frac{\nabla T_i}{T_i} a \right) \quad (2)$$

where B is the magnetic field strength, ρ_i is the ion Larmor radius, a is the plasma minor radius, and C_e , C_i are constant factors that are chosen to fit the experimental result, $C_e = 23.0$ and $C_i = 9.07$.

The state vector is composed of the electron and ion temperature, density, numerical coefficients of turbulent transport models, and heat deposition. The NBI heat deposition is evaluated by GNET-TD [3]. Every state variable is defined on 60 computational grid points (radial direction, 1-D). The time series data of experimentally measured temperature and density profiles are assimilated into TASK3D.

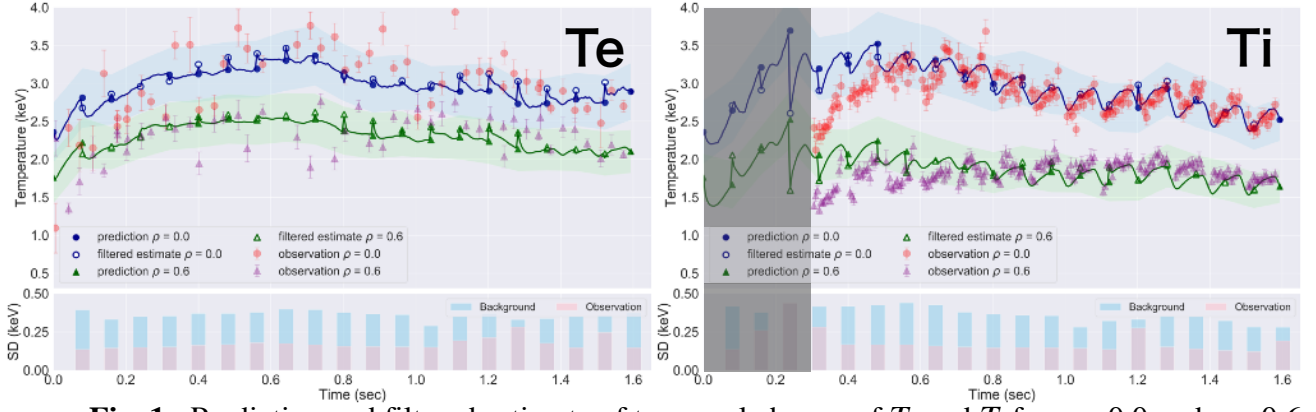


Fig. 1 : Prediction and filtered estimate of temporal change of T_e and T_i for $\rho = 0.0$ and $\rho = 0.6$. Here, ρ is the normalized minor radius. The bar graphs show the estimated standard deviations of background error and observation noise before filtering.

3. Simulation results

We apply the data assimilation system to a typical high ion temperature NBI plasma in LHD (shot:114053). Figure 1 shows the simulation results of T_e and T_i by EnKF, that have been performed with 2000 ensemble members for the cycle of assimilation, $\tau_{DA} = 80$ msec. The assimilation system can accurately reproduce both the electron and ion temperature in terms of those profiles and temporal variations through the optimization of the employed turbulent transport model.

Figure 2 shows the filtered estimate of the numerical coefficient for electron turbulent transport model, C_e . The radial profile have been optimized to reproduce the experimental temperature data, but this estimate is based on only the past data. The EnKS corrects the filtered estimate as Fig. 2 using future data. The smoothed estimate of C_e by the EnKS is shown in Fig. 3. It seems that the position of peak moves in the direction of time axis (form 1.2 sec to 1.0sec). Figure 4 is the simulation results of T_e and T_i by TASK3D using the smoothed estimates of C_e , C_i and the NBI heat deposition. It can be confirmed that the TASK3D simulation using this smoothed estimates can reproduce the experimental temperature data with high accuracy. If the estimates of C for various plasmas can be reproduced by a parametric or nonparametric model, more accurate turbulent transport model can be obtained with relevant physical interpretation.

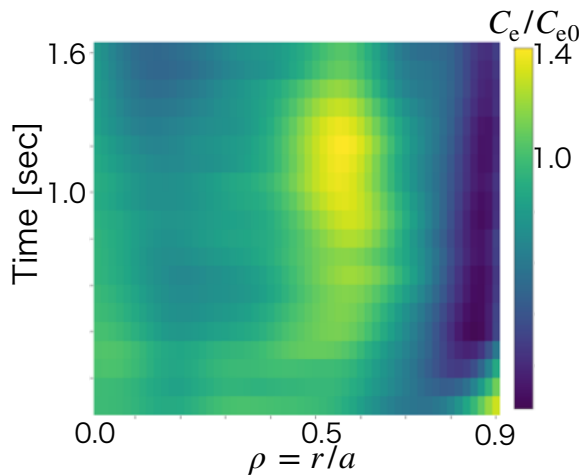


Fig. 2 : Filtered estimate of C_e by EnKF, which are divided by the conventional value, $C_{e0}=23.0$.

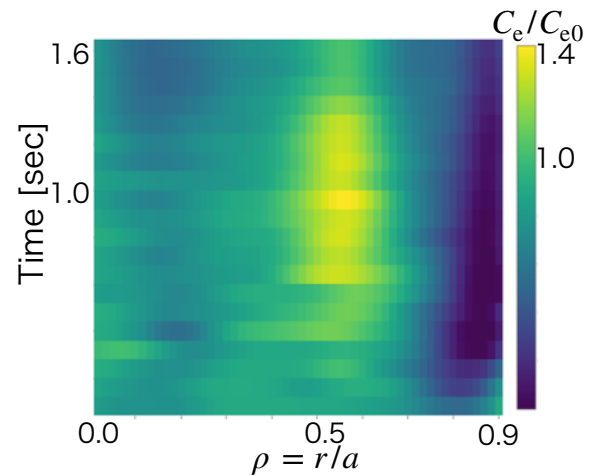


Fig. 3 : Smoothed estimate of C_e by EnKS, which are divided by the conventional value, $C_{e0}=23.0$.

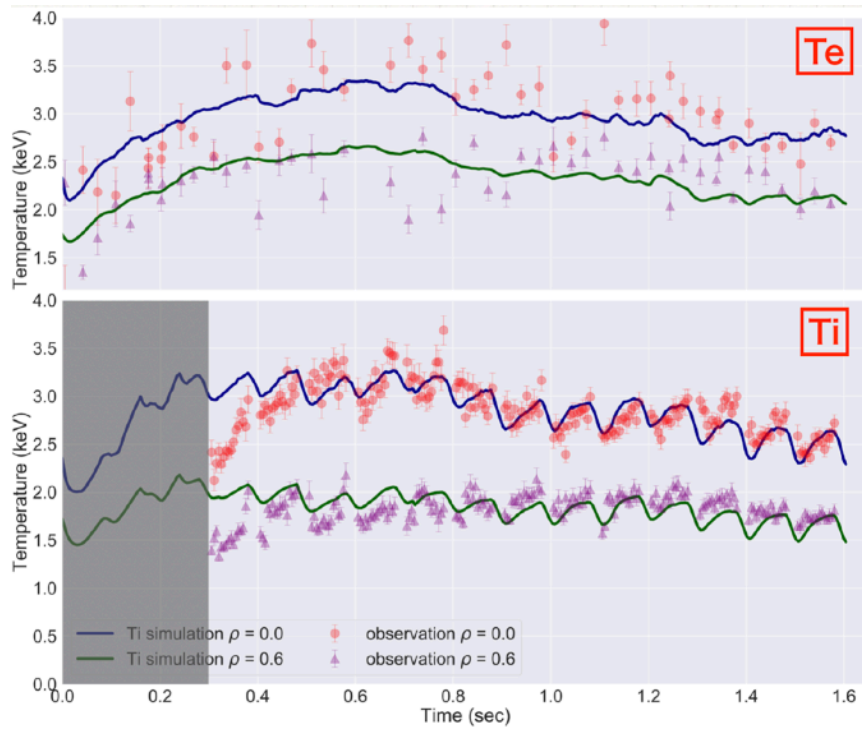


Fig. 4 : Simulation results of temporal change of T_e and T_i for $\rho = 0.0$ and $\rho = 0.6$ using the smoothed estimate of C_e , C_i and the NBI heat deposition.

4. Summary

Data assimilation techniques have been applied to the integrated transport simulation (TASK3D) of a plasma in LHD. We use the EnKF and the EnKS as a data assimilation methods for the estimation of state variables. The time series data of experimentally measured temperature and density profiles have been assimilated into TASK3D. The assimilation system has accurately reproduced both the electron and ion temperature through the optimization of the employed turbulent transport model. These results indicate the effectiveness and validity of the data assimilation approach for accurate prediction of the behavior of fusion plasmas and the possibility of advanced turbulence modeling.

References

- [1] S. Murakami, et al., Plasma Phys. Control. Fusion **57**, 119601 (2015).
- [2] G. Evensen, Ocean Dynamics **53**, 343-367 (2003).
- [3] H. Yamaguchi, et al., Plasma Fusion Res. **8**, 2403099 (2013).

TAE and Alfvén-Slow Eigenmodes in Burning Tokamak Plasmas

C. Z. Cheng

Department of Advanced Energy, University of Tokyo, Japan

Talk presented at BPSI17, held at Kyushu University, December 15-16, 2019

In present tokamak plasma fusion experiments, the auxiliary heating such as neutral beam injection, radio frequency wave heating, etc. are the main heating sources to heat the ions and sustain the plasma steady state operations to counter the energy loss due to anomalous energy transport. However, in burning tokamak plasma reactors, the auxiliary heating methods are insufficient to heat ions and sustain the burning plasma operation. Instead, to maintain plasma in fusion burning condition, ions must be heated by alpha particles, which are produced in the deuterium-tritium (D-T) fusion reaction to maintain plasma temperature ideal for fusion reaction. Presently scientists expect that alpha-particles to be the dominant heating source with alpha heating power $P_\alpha (=W_\alpha/\tau_s)$ larger than the loss power $P_{\text{loss}} (=W_{\text{tot}}/\tau_E)$, where W_α is the alpha particle energy, τ_s is the alpha particle slowing-down time, W_{tot} is the total plasma energy, and τ_E is the energy confinement time. Thus, alpha particles control the thermal plasma profiles, the global plasma stability and the energy and particle confinement. Thus, significant alpha particle loss can quench DT burning, degrades heating and current drive efficiency, and causes localized damage on first wall of fusion reactors. Thus, an important scientific focus of fusion energy research has been the confinement of fast ions and alpha particles.

In mid-1980s the Toroidal Alfvén Eigenmodes (TAE) [1, 2] was discovered theoretically. A brief description of TAE frequency gap and existence of TAE is given in Appendix A. Then, in early 1990s the excitation of TAEs by fast ions was observed in TFTR and DIII-D tokamaks. Since then, many other types of Alfvén eigenmodes such as the Reversed Shear Alfvén Eigenmodes (RSAE) [3-6] have been discovered. The interaction of fast ions with Alfvén eigenmodes have been very actively studied and significant loss of fast ions caused by unstable Alfvén eigenmodes has been observed in almost all major tokamaks such as TFTR, JT-60U, JET, etc. Thus, in burning plasma fusion reactors, the Alfvén eigenmodes are also expected to interact with alpha particles and can possibly cause significant alpha loss from the reactor core. Early D-T experiments in TFTR had identified unstable TAE and RSAE, but with weak growth rate due to small tritium fraction [7, 8]. Thus, no significant alpha loss was reported. However, in burning plasma fusion reactors, large amount of tritium will be used to produce significant fusion power. Thus, fast ion interaction with Alfvén eigenmodes will be a critical research area of burning plasma physics.

Tokamak experiments in high- β plasmas have also revealed new discrete frequency modes with frequencies below the TAE frequency continuum gap and they are called the Beta induced Alfvén Eigenmodes (BAE) [9, 10]. One theory for the BAE is the creation of the beta-induced Alfvén gap, which is just below the lower continuum that defines the TAE gap lower boundary and is obtained by employing the slow mode approximation of the MHD model [11, 12]. However, the slow mode approximation neglects the slow mode propagation physics and is thus not appropriate. Thus, many works were performed to study the frequency gaps due to coupling between the Alfvén wave and slow mode continuous spectra based on the MHD theory and the existence of discrete frequency eigenmodes with frequencies below the TAE gap. Recently we have provided a comprehensive theory of the formation of Alfvén-Slow (AS) frequency gaps and the discovery of many Alfvén-Slow Eigenmodes (ASE) in Tokamaks [13]. The previously identified Beta-induced Alfvén Acoustic Eigenmode (BAAE) [14] is one type of several different discrete ASEs. The existence of ASEs is ubiquitous for normal and reserve safety factor profiles, broad range of plasma β values, different plasma shapes and many different toroidal mode numbers. The newly discovered ASEs provide explanation to the experimentally observed BAE destabilized by fast ions with frequencies below the TAE frequency gap. A simplified explanation of AS gaps and ASEs is given in Appendix B.

With the theoretical discovery of the TAE and ASE, we expect these eigenmodes will be critical for understanding the confinement of alpha particle and fast ions in burning plasma fusion reactors. TAEs were previously studied extensively, but ASEs are just started to be studied. Because ASEs have lower frequency than TAEs, we expect ASEs will interact with lower energy fast ions such as the slowed-down alpha particles called Helium ash and the thermal ions more easily. In the next few years, theoretical and experimental efforts should be addressed to study interaction of fast ions and alpha particles with ASEs and TAEs.

Appendix A: TAE gap and TAEs

The TAEs are created due to the coupling of the shear Alfvén continuous frequency spectrum of neighboring poloidal harmonics such as m and $m+1$ around the $q=(m+1/2)/n$ region, where q is the safety factor, n is the toroidal mode number and m is the poloidal harmonic number [1, 2]. The coupling forms a frequency gap, called TAE gap, in the Alfvén continuous spectrum with frequency as continuous functions of the plasma minor radius and allows global TAEs to exist with frequencies inside the TAE gap. Figure 1 shows (a) frequency $(\omega/\omega_A)^2$ versus plasma minor radius of an $n=1$

mode continuous spectrum and (b) the radius structure of poloidal harmonics of an $n=1$ TAE mode for a circular tokamak with $q(0) = 1.048$ and $q(a)=2.3$, where $\omega_A = V_A(0)/q(0)R$ is a normalized frequency [2]. Because TAE frequency does not intersect with the continuous frequency spectrum, the poloidal harmonic structures are regular functions of radius and thus TAEs do not suffer continuum damping due to phase mixing effect. Thus, TAEs can be destabilized by the free energy of fast ion pressure non-uniformity if the free energy can overcome the Landau damping effects of thermal ions and electrons.

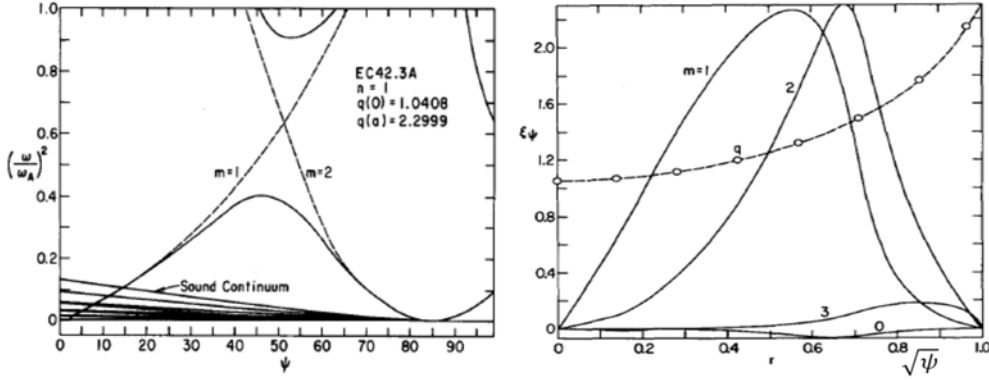


FIG 1 (a) Frequency $(\omega/\omega_A)^2$ versus plasma minor radius of an $n = 1$ mode continuous spectrum, and (b) the radius structure of poloidal harmonics of an $n = 1$ TAE mode for a circular cross-section tokamak with $q(0) = 1.048$ and $q(1)=2.3$. The frequency is normalized by $\omega_A = V_A(0)/q(1)R$, V_A is the Alfvén velocity, and R is the major radius.

Appendix B: Alfvén-Slow Frequency Gaps and Alfvén-Slow Eigenmodes

The Alfvén-Slow (AS) frequency gaps are produced due to the coupling of the shear Alfvén continuous frequency spectrum of m poloidal harmonic and the slow mode continuous spectrum of different m poloidal harmonics [13]. For example, the coupling of the Alfvén m poloidal harmonic and the slow mode $m\pm 1$ harmonics causes the Alfvén m harmonic continuous spectrum to be uplifted from the uncoupled Alfvén spectrum by an amount related to the plasma pressure and the geodesic magnetic field curvature. However, the frequency of one of the slow mode $m\pm 1$ harmonics is reduced by the same pressure-curvature coupling effect, but the frequency of the other slow mode harmonic is relatively unaffected. As a result the Alfvén-Slow mode continuous spectrum is broken up with two Alfvén-Slow (AS) gaps below the TAE continuum gap are shown schematically in Fig. 2. Coupling of the Alfvén m harmonic with the slow mode $m\pm 2$ harmonics also creates additional AS gaps if their frequencies cross each other. The AS

gap widths increase with the plasma pressure. The creation of AS gaps allow the existence of several new types of Alfvén-Slow Eigenmodes (ASE). The radial structure of these new ASEs do not intersect with the continuous spectrum and thus do not suffer continuum damping. An example of the continuous spectrum due to Alfvén-slow mode coupling showing the AS gaps and the existence of six ASEs with discrete frequencies are shown in Fig. 3 for a tokamak equilibrium with $\beta(0) = 5\%$, aspect ratio $R/a = 3$, $q(0) = 1.0$, and $q(1)=2.42$. Note that the discrete modes with frequencies above 200 kHz are TAEs and RSAEs.

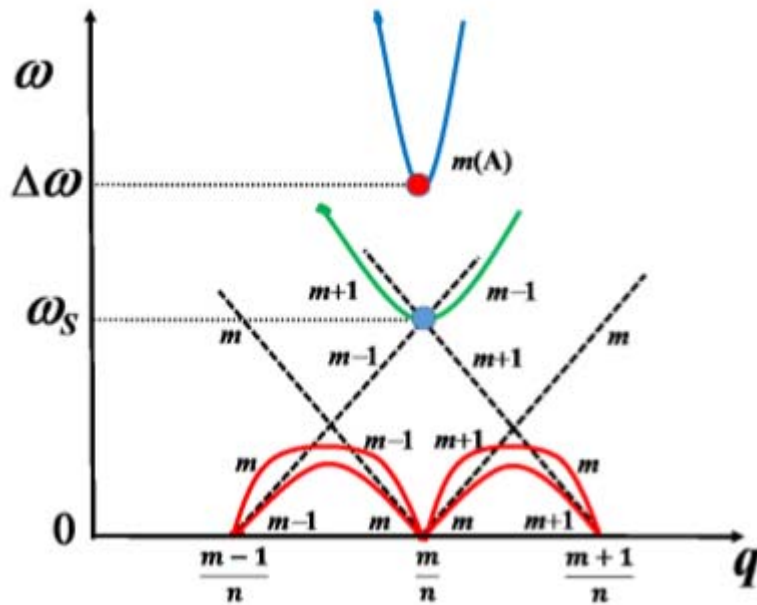


FIG. 2: The continuous spectrum (ω versus q) due to 3-harmonic coupling of the Alfvén m harmonic and the slow mode $m \pm 1$ harmonics is shown schematically. The dashed lines indicate the uncoupled slow mode frequency spectrum. The blue curves indicate the uplifted Alfvén m harmonic continuous spectrum. The green and upper red curves show the coupled slow mode $m \pm 1$ harmonic continuous spectrum. The lower red curves indicate the slow mode m harmonic continuous spectrum.

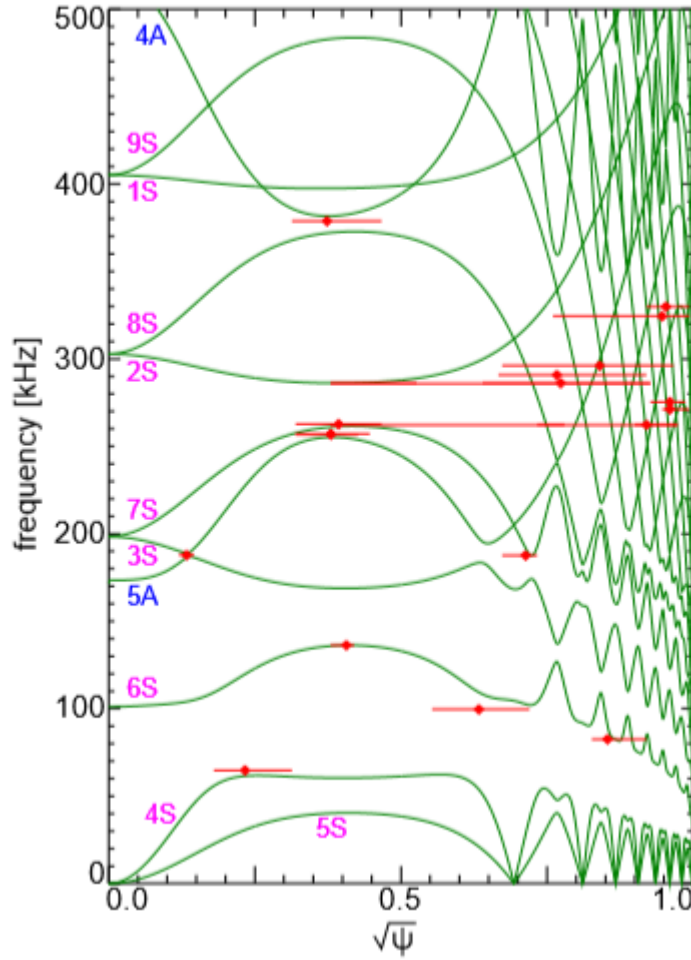


FIG. 3: The continuous spectrum frequency showing AS gaps and the discrete frequencies of ASEs for $n = 5$ mode versus minor radius for a tokamak equilibrium with $\beta(0) = 5\%$, aspect ratio $R/a = 3$, $q(0) = 1.0$, and $q(1) = 2.42$. The red horizontal bars show the frequencies of these discrete ASEs and the amplitude half width in the radial direction with dot indicating the peaking amplitude location. The frequency is calculated by choosing the normalized Alfvén frequency $f_{A0} = B_0/2\pi\rho(0)q(1)R = 214.445$ kHz.

References

- [1] C. Z. Cheng and M. S. Chance, Phys. Fluids 29, 3695 (1986).
- [2] C. Z. Cheng, L. Chen, and M. S. Chance, Annals Phys. 161, 21 (1985).
- [3] H. Kimura, Y. Kusama, M. Saigusa, G.J. Kramer, K. Tobita, M. Nemoto, T. Kondoh, T. Nishitani, O. DA Costa, T. Ozeki, et al., Nucl. Fusion 9, 1303 (1998).
- [4] B. N. Breizman, H. L. Berk, M. S. Pekker, S. D. Pinches, and S. E. Sharapov, Phys. Plasmas 10, 3649 (2003).

- [5] G. J. Kramer, N. N. Gorelenkov, R Nazikian, and C Z Cheng, Plasma Phys. Control. Fusion 46, L23 (2004).
- [6] M. Takechi, A. Fukuyama, M. Ishikawa, C. Z. Cheng, K. Shinohara, T. Ozeki, Y. Kusama, S. Takeji, T. Fujita, T. Oikawa, et al., Phys. Plasmas 12, 082509 (2005).
- [7] R. Nazikian, et al., Phys. Rev. Lett. 78, 2976 (1997).
- [8] R. Nazikian, G. J. Kramer, C. Z. Cheng, N. N. Gorelenkov, H. L. Berk, and S. E. Sharapov, Phys. Rev. Lett. 91, 125003 (2003).
- [9] W. W. Heidbrink, E. Ruskov, E. M. Carolipio, J. Fang, M. A. van Zee eland, and R. A. James, Phys. Plasmas 6, 1147 (1999).
- [10] W. W. Heidbrink, Phys. Plasmas 15, 055501 (2008).
- [11] A. D. Turnbull, E. J. Strait, W. W. Heidbrink, M. S. Chu, H. H. Duong, J. M. Greene, L. L. Lao, T. S. Taylor, and S. J. Thompson, Phys. Fluids B 5, 2546 (1993).
- [12] M. S. Chu, J. M. Greene, L. L. Lao, A. D. Turnbull, and M. S. Chance, Phys. Fluids 4, 3713 (1992).
- [13] C. Z. Cheng, G. J. Kramer, M. Podesta, R. Nazikian, Phys. Plasmas 26, 082508 (2019)
- [14] N. N. Gorelenkov, H. L. Berk, N. A. Crocker, E. D. Fredrickson, S. Kaye, S. Kubota, H. Park, W. Peebles, S. A. Sabbagh, S. E. Sharapov, et al., Plasma Phys. Control. Fusion 49, B371 (2007).

Extraction of spatial structures of intermittent events using dynamical mode decomposition

^{1,2}M. Sasaki, ³Y. Kawachi, ^{2,4,5}R. O. Dendy, ⁶H. Arakawa, ^{1,2}N. Kasuya,
⁷F. Kin, ¹K. Yamasaki, ^{1,2}S. Inagaki

¹ *Research Institute for Applied Mechanics, Kyushu University, Japan*

² *Research Center for Plasma Turbulences, Kyushu University, Japan*

³ *Interdisciplinary Graduate School of Engineering Sciences, Kyushu University, Japan*

⁴ *Department of Physics, Warwick University, Coventry UK*

⁵ *CCFE, Culham Science Centre, Oxford UK*

⁶ *Institute of Science and Engineering, Academic Assembly, Shimane University, Japan*

⁷ *National Institutes for Quantum and Radiological Science and Technology, Japan*

Intermittent events in turbulence are ubiquitous in fluids; the solar flare [1], the torrential heavy rain [2], ocean current, and so on. In magnetized plasmas, intermittent events frequently occurs, such as the edge localized modes (ELMs), and blobs, which significantly affect the properties of plasmas. These intermittent events are caused nonlinearly, so that the spatio-temporal properties usually involve higher harmonics. Therefore, the number of degrees of freedom that play roles in intermittent events increases when the Fourier mode decomposition is applied. In order to understand the nonlinear properties of such events, it is important to extract spatio-temporal structures with reducing the degrees of freedom as much as possible.

In this study, the dynamical mode decomposition (DMD) is applied to turbulence simulation data [3], in order to extract the spatio-temporal behavior of the intermittent or transient events with reducing the number of degrees of freedom. The DMD method is used, which does not assume any functional form for the structure. Only based on observed signals, spatio-temporal patterns that are statistically valid are derived from the eigenvalue problem. The turbulence simulation we use is a direct numerical simulation in cylindrical magnetized plasmas, and the nonlinear dynamics of the Kelvin-Helmholtz instability are self-consistently calculated. Using the turbulence simulation, where all the three dimensional turbulence informations are known, the intermittent or transient dynamics of the turbulence is decomposed by the DMD method. The obtained DMD modes comprise rotationally symmetric deformations together with spiral patterns. A new method to calculate the time evolution of DMD mode amplitudes is proposed, based on convolution-type correlation integrals, and then applied to the simulation outputs in a limit cycle regime. The resulting time traces capture the essential physics far better than Fourier techniques applied to the same data [4].

[1] N. Scafetta, et. al., Phys. Rev. Lett. 90, 248701 (2003).

[2] N. Takahashi, et. al., Journal of Disaster Research, 14, 235 (2019).

[3] M. Sasaki, et. al., Phys. Plasmas, 26, 042305 (2019).

[4] M. Sasaki, et. al., Plasma Phys. Control. Fusion, 61, 112001 (2019).

Statistical induction of a thermal transport model of fusion plasmas based on the transport analysis database

Masayuki Yokoyama^{1,2}

¹ National Institute for Fusion Science, National Institutes of Natural Sciences,

² The Graduate University for Advanced Studies (SOKENDAI),

322-6 Oroshi, Toki 509-5292, Japan

yokoyama@nifs.ac.jp

A statistical induction of a thermal transport model of fusion plasmas has been conducted by regression analysis utilizing the accumulated experimental transport analysis database [1]. This approach is unique and simple in a sense that it does not require any detailed physics modelling such as neoclassical and turbulent transport. It has come to the stage to elucidate the influential physics quantities to prescribe the heat diffusivity, and to compare/interpret experimentally identified trends. This progress will foster acquiring practical transport models for a real-time control and the guidance to the parameter dependence to be elucidated through large-scale cutting-edge simulations.

The thermal transport analysis database considered in this study is the same as that used in Ref. [2], as reproduced in Figure 1. This is the database (about 3000 data) for the ion thermal diffusivity, χ_{i} , constructed from 31 discharges (so-called high-ion-temperature (T_i) scenario) in Large Helical Device (LHD) [3]. The database was constructed by the integrated transport analysis suite, TASK3D-a [4] to LHD plasmas.

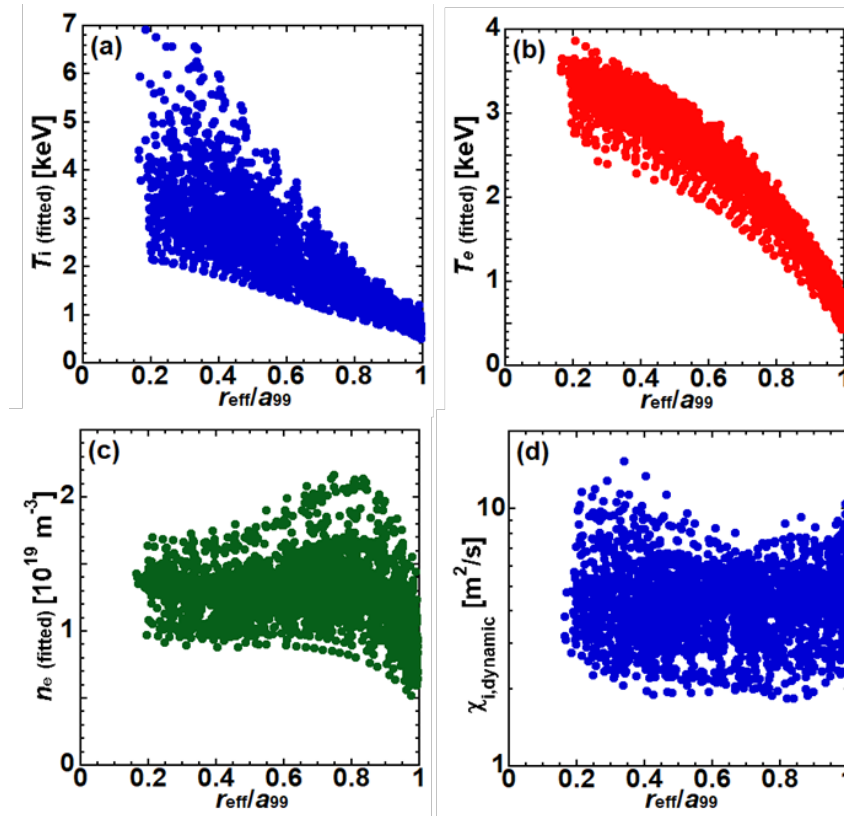


Fig. 1: All the data points of employed database (LHD high- T_i (ion temperature) scenario) for (a) T_i , (b) T_e (electron temperature), (c) n_e (electron density) and then (d) χ_{i} , which are reproduced from Ref. [2].

The log(10)-linear multivariate regression analysis was performed on this database. When it comes to a physics interpretation of the regression result, keeping a smaller number of variables with larger influence is more transparent. For this, the database for $r_{\text{eff}}/a_{99} < 0.35$ (404 data, roughly inside ion internal transport barrier [5]) is employed in the following discussion. Here, a_{99} is a measure of the experimentally known last closed flux surface, defined by the effective minor radius which encloses 99% of the total electron pressure (requiring pre-calculated VMEC equilibrium database, and r_{eff} is the minor radius defined by the radius of the equivalent simple torus which encloses the same volume as the flux surface of interest [6].

The AIC (Akaike's Information Criterion) [7] is the measure for the relative quality of statistical models for a given dataset. Practically, the minimum (or the lowest) AIC selects an "optimal" model among many candidates. More precisely, AICc (AIC with a correction for small sample sizes) [8] is used. Based on the AICc analysis, the regression expression with 4 variables (selected out of initially considered 9 variables [1]),

$$\frac{\chi_i}{r_{\text{eff}}^2 \omega_i} = 10^{-0.066} \rho_i^{*2.79} (T_e/T_i)^{2.32} (R/L_{Ti})^{-0.94} \epsilon_h^{-0.58}$$

is obtained, where, R/L_{Ti} and ϵ_h are the ion collision frequency normalized by its banana-plateau boundary, the scale length of the ion temperature gradient with R being the vacuum magnetic axis position and the main helicity of magnetic configuration, respectively. It should be noted that this expression is only valid for dataset of $r_{\text{eff}}/a_{99} < 0.35$ of the database shown in Fig. 1, due to the inherent nature of regression analysis.

Positive value of power of ρ_i^* indicates χ_i gets larger as T_i becomes higher. However, power of T_i becomes negative if ρ_i^* and T_e/T_i considered simultaneously. The ϵ_h itself currently does not cover any of changes of magnetic configurations, however, its exclusion worsens the goodness. The negative power of R/L_{Ti} would be physically interpreted as that the ion heat diffusivity in ion internal transport barrier decreases as the ion temperature gradient becomes larger (or its scale length becomes smaller making R/L_{Ti} larger) [5]. The increase of heat diffusivity (then the decrease of the ion temperature gradient) for increasing T_e/T_i has also been recognized experimentally in LHD [9].

Based on these considerations, the induced regression expression statistically resolves complicated entanglements among T_i , T_e/T_i and its gradient (R/L_{Ti}), and the feature of transport barrier formation, in a single line expression.

It would be interesting to consider this kind of regression results to compare with simulations when results for substantial number of time slices in LHD are accumulated. Also, transport analysis datasets in other operational scenario/other experiments (worldwide) could provide a new insight for thermal transport modelling of fusion plasmas, complementing conventional global scalings for the energy confinement time.

References

- [1] M. Yokoyama. Nucl. Fusion 59 (2019) 094004. (Corrigendum: Nucl. Fusion 60 (2020) 029501.
- [2] M. Yokoyama et al., Plasma Fusion Res. 9 (2014) 1302137.
- [3] Y. Takeiri et al., Nucl. Fusion 57 (2017) 102023.
- [4] M. Yokoyama et al., Nucl. Fusion 57 (2017) 126016.
- [5] K. Nagaoka et al., Nucl. Fusion 59 (2019) 100602.
- [6] C. Suzuki et al., Plasma Phys. Control. Fusion 55 (2013) 014016.
- [7] H. Akaike, "Information theory and an extension of the maximum likelihood principle", Proceedings of the 2nd International Symposium on Information Theory, Petrov, B. N., and Caski, F. (eds.), Akademiai Kiado, Budapest (1973) 267.
- [8] N. Sugiura, Communications in Statistics - Theory and Methods 7 (1978) 13.
- [9] H. Takahashi et al., Nucl. Fusion 57 (2017) 086029.